1 # Global retrieval of TROPOMI tropospheric HCHO and NO₂

2 # columns with improved consistency based on updated Peking

3 # University OMI NO₂ algorithm

4 Yuhang Zhang[1,2], Huan Yu[2], Isabelle De Smedt[2], Jintai Lin[1], Nicolas Theys[2], Michel Van
5 Roozendael[2], Gaia Pinardi[2], Steven Compernolle[2], Ruijing Ni[3], Fangxuan Ren[1], Sijie Wang[1],
6 Lulu Chen[1], Jos Van Geffen[4], Mengyao Liu[4], Alexander M. Cede[5], Alexis Merlaud[2], Martina
7 M. Friedrich[2], Andreas Richter[6], Ankie Piters[4], Vinod Kumar[3,7], Vinayak Sinha[7], Thomas
8 Wagner[3], Yongjoo Choi[8], Hisahiro Takashima[9], Yugo Kanaya[10], Hitoshi Irie[11], Robert Spurr[12],
9 Wenfu Sun[2], Lorenzo Fabris[2]

10 [1]Laboratory for Climate and Ocean-Atmosphere Studies, Department of Atmospheric and Oceanic Sciences,
11 School of Physics, Peking University, Beijing 100871, China
12 [2]Royal Belgian Institute for Space Aeronomy, BIRA-IASB, Ringlaan 3, 1180 Uccle, Belgium
13 [3]Max Planck Institute for Chemistry, Mainz 55128, Germany
14 [4]Royal Netherlands Meteorological Institute (KNMI), Utrechtseweg 297, 3730 AE De Bilt, the Netherlands
15 [5]NASA Goddard Space Flight Center, Greenbelt, MD 20771, USA
16 [6]Institute of Environmental Physics (IUP), University of Bremen, Otto-Hahn-Allee 1, Bremen 28359, Germany
17 [7]Department of Earth and Environmental Sciences, Indian Institute of Science Education and Research, Mohali,
18 Punjab, India
19 [8]Hankuk University of Foreign Studies, Yongin, Republic of Korea
20 [9]Fukuoka University, Fukuoka, Japan
21 [10]Research Institute for Global Change, Japan Agency for Marine-Earth Science and Technology (JAMSTEC),
22 Yokohama, Japan
23 [11]Center for Environmental Remote Sensing, Chiba University (Chiba U), Chiba, Japan
24 [12]RT Solutions Inc., Cambridge, MA 02138, USA

25 *Correspondence to*: Jintai Lin (linjt@pku.edu.cn), Michel Van Roozendael (michel.vanroozendael@aeronomie.be)

26 **Abstract.** The TROPOspheric Monitoring Instrument (TROPOMI), onboard the Sentinel-5 Precursor (S5P)

27 satellite launched in October 2017, is dedicated to monitoring the atmospheric composition associated with air

28 quality and climate change. This paper presents the global retrieval of TROPOMI tropospheric formaldehyde

29 (HCHO) and nitrogen dioxide (NO₂) vertical columns using an updated version of the Peking University OMI

30 NO₂ (POMINO) algorithm, which focuses on improving the calculation of air mass factors (AMFs). The algorithm

31 features explicit corrections for the surface reflectance anisotropy and aerosol optical effects, and uses daily high-

32 resolution (0.25º×0.25º) a priori HCHO and NO₂ profiles from the Global Earth Observing System Composition

33 Forecast (GEOS-CF) dataset. For cloud correction, a consistent approach is used for both HCHO and NO₂

34 retrievals, where (1) the cloud fraction is re-calculated at 440 nm using the same ancillary parameters as those

35 used in the NO₂ AMF calculation, and (2) the cloud top pressure is taken from the operational FRESCO-S cloud

36 product.

37 The comparison between POMINO and reprocessed (RPRO) operational products in April, July, October 2021

38 and January 2022 exhibits high spatial agreement, but RPRO tropospheric HCHO and NO₂ columns are lower by

39 10% to 20% over polluted regions. Sensitivity tests with POMINO show that the HCHO retrieval differences are

40 mainly caused by different aerosol correction methods (implicit versus explicit), prior information of vertical

41 profile shapes and background corrections; while the NO₂ retrieval discrepancies result from different aerosol

42 corrections, surface reflectances and a priori vertical profile shapes as well as their non-linear interactions. With

43 explicit aerosol corrections, the HCHO structural uncertainty due to the cloud correction using different cloud

44   parameters is within ± 20%, mainly caused by cloud height differences. Validation against ground-based

45   measurements from global Multi-Axis Differential Optical Absorption Spectroscopy (MAX-DOAS) observations

46   and the Pandonia Global Network (PGN) shows that in April, July, October 2021 and January 2022, POMINO

47   retrievals present a comparable day-to-day correlation but a reduced bias compared to the RPRO products (HCHO:

48    $R = 0.62$, NMB = −30.8% versus $R = 0.68$, NMB = −35.0%; NO_2: $R = 0.84$, NMB = −9.5% versus $R = 0.85$,

49   NMB = −19.4%). An improved agreement of $HCHO/NO_2$ ratio (FNR) with PGN measurements based on

50   POMINO retrievals is also found ($R = 0.83$, NMB = −18.4% versus $R = 0.82$, NMB = −24.1%). Our POMINO

51   retrieval provides a useful source of information particularly for studies combining HCHO and NO_2.

52   **1 Introduction**

53   Formaldehyde (HCHO) and nitrogen dioxide (NO_2) are important trace gases in the troposphere. They play a

54   critical role in the processes of tropospheric ozone (O_3) and aerosol formation, and have significant influences on

55   air quality, climate and human health (Beelen et al., 2014; Crutzen, 1970; Shindell et al., 2009). Methods to

56   retrieve tropospheric HCHO and NO_2 vertical column densities (VCDs), respectively in the ultraviolet (UV) and

57   visible (VIS) spectral ranges, have rapidly developed in the last decades, based on sensors mounted on both sun-

58   synchronous and geostationary satellites such as the Global Ozone Monitoring Experiment (GOME; Burrows et

59   al., 1999), SCanning Imaging Absorption spectroMeter for Atmospheric CHartographY (SCIAMACHY;

60   Bovensmann et al., 1999), Ozone Monitoring Instrument (OMI; Levelt et al., 2006), Global Ozone Monitoring

61   Experiment-2 (GOME-2; Callies et al., 2000), TROPOspheric Monitoring Instrument (TROPOMI; Veefkind et

62   al., 2012), Environmental Trace Gases Monitoring Instrument (EMI; Zhang et al., 2020) and Geostationary

63   Environment Monitoring Spectrometer (GEMS; Kim et al., 2020). Such satellite observations have been

64   extensively used in studies related to long-term trend and variabilities (De Smedt et al., 2010; Jiang et al., 2022;

65   Richter et al., 2005), estimation of surface-level concentrations (Cooper et al., 2022; Wei et al., 2022), constraining

66   emissions of non-methane volatile organic compounds (NMVOCs) and nitrogen oxides ($NO_x \equiv NO + NO_2$) (Kong

67   et al., 2022; Lin, 2012; Stavrakou et al., 2018), non-linear ozone chemistry (Jin et al., 2017, 2023; Jin and

68   Holloway, 2015) and impacts on the environment and human health (Chen et al., 2022; Li et al., 2023).

69   The retrieval algorithms of tropospheric HCHO and NO_2 VCDs based on observations from spaceborne

70   instruments share many retrieval concepts. First, the slant column density (SCD) representing the trace gas

71   concentration integrated along the average light path is obtained by performing a spectral fit from backscattered

72   radiance and irradiance spectra. Second the SCD is converted to a VCD using air mass factors (AMFs) obtained

73   from radiative transfer (RT) calculations, which are a function of the observation geometry, cloud information,

74   aerosol properties, surface conditions and the shape of a priori vertical profiles. The main intrinsic differences

75   between HCHO and NO_2 retrievals are that (1) different wavelength ranges are used for each retrieval, and (2) the

76   final tropospheric HCHO VCDs are determined with additional background correction based on modelled HCHO

77   columns in the reference region in the Field of Regard (FOR) of satellite instruments, while for NO_2 a stratosphere-

78   troposphere separation is performed before AMF application to obtain tropospheric columns.

79   Many studies have focused on improving or developing retrieval algorithms to generate scientific HCHO or NO_2

80   products for comparison with operational products and for applications (e.g., Liu et al., 2020; Liu et al., 2021; Su

81   et al., 2020). However, little attention has been paid to fixing the systematic differences in ancillary parameters

82   between HCHO and NO_2 AMF calculations. For instance, the TROPOMI reprocessed (RPRO) HCHO version

83   2.4.1 and NO_2 version 2.4.0 operational products make use of cloud information from different sources: the

84   Optical Cloud Recognition Algorithm/Retrieval of Cloud information using Neural Networks (OCRA/ROCINN)

85   - Cloud as Reflecting Boundaries (CRB) product is used for HCHO, while the Fast Retrieval Scheme for Clouds

86   from Oxygen absorptions bands - Sentinels (FRESCO-S) product is used for NO_2. Besides, the surface albedo

87   used in the current HCHO retrieval is the OMI-based monthly minimum Lambertian-equivalent reflectivity

88   (MLER) at 340 nm with a spatial resolution of $0.5º \times 0.5º$ (lat. $\times$ long.), whereas the one used in the NO_2 retrieval

89   has been updated with the KNMI TROPOMI directionally dependent Lambertian-equivalent reflectivity (DLER)

90   v1.0 database at 440 nm with a spatial resolution of $0.125º \times 0.125º$. Finally, the radiative transfer model used for

91   HCHO AMF calculation is the linearized pseudo-spherical scalar and vector discrete ordinate radiative transfer

92   code (VLIDORT) version 2.6, whereas that used for NO_2 AMF calculation is the Double-Adding KNMI (DAK)

93   polarized radiative transfer code version 3.2. Such inconsistencies are an important limitation for studies

94   combining satellite HCHO and NO_2 products, such as analysis of ozone chemistry and wildfires (Jin et al., 2020,

95   2023). Therefore, there is a need for consistent retrievals of tropospheric HCHO and NO_2 VCDs. Moreover, the

96   TROPOMI operational HCHO and NO_2 products do not explicitly account for the optical effect of aerosols, and

97   use a priori profile shapes from the massively parallel version of the Tracer Model 5 (TM5-MP; Williams et al.,

98   2017) with a relatively coarse spatial resolution ($1º \times 1º$).

99   The Peking University OMI NO_2 (POMINO) algorithm offers a potential tool to address these limitations.

100   Founded by Lin et al. (2014), POMINO has been continuously developed and applied to the OMI, TROPOMI and

101   GEMS instruments (Lin et al., 2014, 2015; Liu et al., 2019, 2020; Zhang et al., 2023). POMINO features an

102   explicit treatment of aerosol optical effects and surface reflectance anisotropy, as well as a re-calculation of cloud

103   information using ancillary parameters consistent with those used for NO_2 AMF calculation. A smaller bias of

104   POMINO NO_2 data than the operational products has been reported from validation against independent ground-

105   based measurements (Liu et al., 2019, 2020; Zhang et al., 2023). However, the previous POMINO-TROPOMI

106   algorithm was limited to Asia, and its potential for HCHO retrieval remained unexplored.

107   In this paper, we present the global retrieval of TROPOMI tropospheric HCHO and NO_2 VCDs with much

108   improved consistency, based on an updated version of the POMINO algorithm. After describing the methods and

109   data in Section 2, we present the quantitative comparison of tropospheric HCHO and NO_2 columns between

110   POMINO and RPRO products (Sect. 3). We then discuss the structural uncertainty of HCHO and NO_2 retrieval

111   based on the POMINO algorithm, by conducting a series of sensitivity tests on cloud correction, aerosol correction,

112   surface reflectance and a priori profile shapes (Sect. 4). Tentative estimates of POMINO retrieval uncertainty are

113   given in Sect. 5. Finally, we use independent ground-based measurements from a global network of Multi-Axis

114   Differential Optical Absorption Spectroscopy (MAX-DOAS) instruments and the Pandonia Global Network

115   (PGN) to validate the tropospheric HCHO and NO_2 columns from the POMINO and RPRO products (Sect. 6).

116   **2 Method and data**

117   **2.1 TROPOMI instrument and operational algorithms for HCHO and NO_2 retrieval**

118   TROPOMI is an imaging spectrometer onboard the European Space Agency (ESA) Copernicus Sentinel-5

119   Precursor (S5P) satellite launched on 13th October 2017, crossing the equator at around 13:30 local time (LT)

120   (Veefkind et al., 2012). Its wide spectral range includes the ultraviolet (UV), visible (VIS), near-infrared (NIR)

Atmospheric
Measurement
Techniques
Discussions

Open Access

EGU

121 and shortwave infrared (SWIR), allowing monitoring of atmospheric trace gases, aerosols, clouds and surface

122 properties. The original spatial resolution of 7 km × 3.5 km (along-track × across-track) at nadir was refined to

123 5.5 km × 3.5 km on the 6th of August 2019 by means of a reduction of the along-track integration time. The wide

124 swath of about 2600 km in the across-track direction enables global coverage on a daily basis.

125 The TROPOMI operational HCHO and NO_2 retrieval algorithms have been fully described in De Smedt (2022)

126 and Van Geffen et al. (2022b), respectively. The first common step is to derive slant columns by performing a

127 spectral fit using the Differential Optical Absorption Spectroscopy (DOAS) method. Specifics for the SCD

128 retrieval are provided in Table S1. After the DOAS spectral fitting, a two-step normalization of the HCHO slant

129 columns is performed to remove any remaining global offset and possible stripes. Then the corrected differential

130 SCDs (dSCDs) are converted to vertical columns using AMFs at 340 nm. The AMFs are derived from a pre-

131 calculated look-up table (LUT) storing altitude-dependent AMFs calculated with the VLIDORT v2.6 radiative

132 transfer model (Table 1). This approach implements implicit aerosol corrections by assuming that aerosols can be

133 simply treated as "effective clouds", and uses the OMI-based monthly MLER dataset for surface reflectance. The

134 HCHO vertical profile shape is specified from TM5-MP daily analyses. For pixels with partly cloudy scenes, a

135 cloud correction is applied based on the independent pixel approximation (IPA) (Martin et al., 2002), using cloud

136 fraction (CF), cloud top pressure (CP) and cloud albedo information from the OCRA/ROCINN-CRB product:

$$ M = w \cdot M_{\text{cld}} + (1 - w) \cdot M_{\text{clr}} \tag{1} $$

138 In Eq. (1), w is the cloud radiance fraction (CRF), M_{cld} the cloudy-sky AMF and M_{clr} the clear-sky AMF. In the

139 final step, TM5-MP HCHO vertical columns in the reference region are added as the compensation for the

140 background HCHO from methane (CH_4) oxidation in the equatorial Pacific. The final tropospheric HCHO VCD,

141 N_V, can be written as follows:

$$ N_V = \frac{N_S - N_{S,0}}{M} + \frac{M_{clear,0}}{M} N_{V,0}^{\text{TM5-MP}} \tag{2} $$

143 with ($N_S - N_{S,0}$) being the corrected HCHO differential slant column, M the HCHO AMF, $M_{clear,0}$ the HCHO clear-

144 sky AMF in the reference region ([90ºS, 90ºN], [180ºW, 120ºW]), and $N_{V,0}^{\text{TM5-MP}}$ the HCHO vertical column from

145 a daily latitude-dependent polynomial, which is fitted through 5° latitude bin means of TM5-MP HCHO vertical

146 columns in the reference region (De Smedt, 2022).

147 For NO_2, a de-striping is also applied to the fitted slant columns even though the systematic across-track features

148 are very small (Van Geffen et al., 2020). The second step is the stratosphere-troposphere separation, where TM5-

149 MP is used to assimilate TROPOMI total NO_2 SCDs, determine the stratospheric NO_2 SCDs and, by subtraction,

150 infer the tropospheric NO_2 SCDs. To calculate tropospheric NO_2 AMFs, the operational algorithm applies implicit

151 aerosol corrections, uses NO_2 a priori profile shapes from TM5-MP daily analyses, and adopts a DLER at 440 nm

152 from the KNMI TROPOMI DLER v1.0 surface reflectance database. For the cloud correction, it takes the cloud

153 top pressure from the FRESCO-S product and retrieves an effective cloud fraction (ECF) by fitting the observed

154 continuum reflectance to a simulated reflectance at 440 nm, assuming an optically thick Lambertian cloud with a

155 fixed cloud albedo of 0.8. The tropospheric NO_2 VCD, N_V^{trop}, can be written as follows:

$$ N_V^{\text{trop}} = \frac{N_S^{\text{total}} - N_S^{\text{strat}}}{M} \tag{3} $$

157 with ($N_S^{\text{total}} - N_S^{\text{strat}}$) the tropospheric NO_2 slant column and M the tropospheric NO_2 AMF.

2.2 Improved POMINO-TROPOMI algorithm for global HCHO and NO$_2$ AMF calculations

Focusing on the improvement of global HCHO and NO$_2$ AMF calculations as well as their consistency, we use an updated POMINO-TROPOMI parallelized AMFv6 package (Figure S1) driven by the LInearized Discrete Ordinate Radiative Transfer code (LIDORT) version 3.6 directly inherited from previous POMINO products (Liu et al., 2020). POMINO calculates the AMFs with online pixel-by-pixel RT simulations rather than using the LUT. As listed in Table 1, explicit aerosol corrections are implemented at the corresponding wavelengths of HCHO and NO$_2$, respectively, based on the aerosol information from Global Earth Observing System Composition Forecast (GEOS-CF; Keller et al., 2021) v1.0 and Moderate Resolution Imaging Spectroradiometer (MODIS) satellite data. We convert GEOS-CF vertical volume mixing ratio profiles to optical depth profiles for each aerosol type, i.e., dust, sulfate-nitrate-ammonium (SNA), organic carbon (OC), black carbon (BC) and sea salt, by using high-spectral-resolution aerosol optical parameters from the GEOS-Chem website (https://ftp.as.harvard.edu/gcgrid/data/aerosol_optics/hi_spectral_res/v9-02/, last access: 23 July 2024). We then convert component-specific aerosol information to vertical profiles of aerosol extinction coefficient, single scattering albedo and phase function. We further use monthly aerosol optical depth (AOD) data from MODIS/Aqua Collection 6.1 MYD04_L2 dataset, with spatial and temporal interpolation for missing values, to constrain the model AOD (Lin et al., 2014). Daily a priori HCHO and NO$_2$ profile shapes at TROPOMI overpass time are also obtained from GEOS-CF v1.0 at the spatial resolution of 0.25º × 0.25º.

In NO$_2$ AMF calculations, to account for the surface reflectance anisotropy over lands and coastal ocean regions, we use bidirectional reflectance distribution function (BRDF) coefficients around 470 nm (band 3; bandwidth: 459 – 479 nm) from the MODIS MCD43C2.006 dataset. The reason for the choice of MODIS BRDF over KNMI TROPOMI DLER is that the operational MODIS BRDF algorithm fully characterizes the dependence of surface reflectance on the solar zenith angle (SZA), viewing zenith angle (VZA) and relative azimuth angle (RAA) by a linear combination of an isotropic parameter plus the volumetric and geometric scattering kernels (Roujean et al., 1992; Zhou et al., 2010), while the DLER model only considers the satellite viewing angle (Tilstra et al., 2024). For HCHO, given that the UV spectral band is not included in the MODIS instrument, we decided to use the climatological DLER at 340 nm from the KNMI TROPOMI DLER v2.0 database.

To allow a consistent cloud correction, we use the same cloud information for both HCHO and NO$_2$ AMF calculation. For each pixel, we acquire the cloud parameters by (1) taking the cloud top pressure from the FRESCO-S cloud product, and (2) re-calculating the cloud fraction at 440 nm in a similar way as used in the operational NO$_2$ algorithm. To simulate the TOA reflectance at 440 nm to derive cloud fraction, we use the ancillary parameters fully consistent with those used in NO$_2$ AMF calculation, i.e., a surface reflectance derived from MODIS BRDF coefficients and explicit aerosol information. Previous studies have demonstrated that in most cases, explicit aerosol corrections lead to reduced cloud (radiance) fractions, especially over regions with heavy aerosol loads such as the North China Plain in winter (Lin et al., 2015); while over regions where frequent aerosol-cloud overlap occurs such as Southeast China in spring, the explicit corrections for absorbing aerosols overlying the cloud deck lead to increased cloud fraction (Jethva et al., 2018). Such differences are because the optical effects of aerosols are separated from those of clouds.

Based on the POMINO structure, we implemented a series of sensitivity tests to assess the importance of structural uncertainties that arise when different ancillary parameters or methodologies are applied to the same data. For HCHO, we first conducted the test "Fst_ORcp" (Case F1) by (1) re-calculating the cloud fraction at 340 nm based

Atmospheric
Measurement
Techniques
Discussions
Open Access
EGU

198 on the reflectance derived using TROPOMI L1B radiance dataset version 2.1 in TROPOMI spectral band 3 (305-

199 400 nm), and irradiance dataset version 2.1 for the Ultra-violet, Visible and Near-Infrared (UVN) module post-

200 processed by BIRA-IASB, and (2) using the cloud top pressure from OCRA/ROCINN-CRB product. Therefore,

201 the differences between POMINO HCHO columns (Case F0) and those of the test "Fst_ORcp" represent the

202 structural uncertainty from the cloud correction using different cloud products. Based on the test "Fst_ORcp", we

203 separately evaluate the effect of aerosol correction, surface reflectance and a priori profile shapes by conducting

204 the tests "Fst_imaer" (Case F2), "Fst_mler" (Case F3) and "Fst_tm5" (Case F4), respectively. Note that in all

205 sensitivity tests, only HCHO AMFs are changed accordingly, while we keep using GEOS-CF HCHO columns for

206 background correction.

207 Similarly, for NO_2 AMF calculations, based on POMINO NO_2 retrievals as the reference (Case N0), tests

208 "Nst_imaer" (Case N1), "Nst_dler" (Case N2) and "Nst_tm5" (Case N3) are used to quantify the individual effect

209 of aerosol correction, surface reflectance and a priori profile shapes. However, we noticed that the NO_2 differences

210 between POMINO and RPRO products can hardly be explained by the linear combination of the individual effect

211 of each ancillary parameter as in the HCHO analysis. Therefore, we further conducted an additional test "Nst_joint"

212 (Case N4) to "mimic" the AMF calculation in the RPRO algorithm, quantifying the joint effect of implicit aerosol

213 corrections, KNMI TROPOMI DLER and TM5-MP a priori NO_2 profile shapes.

214 **Table 1.** Comparison of ancillary parameters between POMINO and RPRO operational products, and sensitivity tests on the
215 corresponding ancillary parameters (highlighted in boldface).

Species	Product or sensitivity test case	RT model	Aerosol correction	Surface reflectance	Cloud correction	A priori profiles
HCHO	RPRO v2.4.1	VLIDORT v2.6 (LUT)	Implicit	OMI-based monthly MLER at 340 nm	CF and CP: OCRA/ROCINN-CRB	Daily TM5-MP (1° × 1°)
	POMINO (Case F0)	LIDORT v3.6 (online)	Explicit	KNMI TROPOMI v2.0 DLER at 340 nm(1)	CF: re-calculated at 440 nm CP: FRESCO-S	Daily GEOS-CF (0.25° × 0.25°)
	Fst_ORcp (Case F1)	LIDORT v3.6 (online)	Explicit	KNMI TROPOMI v2.0 DLER at 340 nm(1)	**CF: calculated at 340 nm** **CP: OCRA/ROCINN-CRB**	Daily GEOS-CF (0.25° × 0.25°)
	Fst_imaer (Case F2)	LIDORT v3.6 (online)	**Implicit**	KNMI TROPOMI v2.0 DLER at 340 nm(1)	CF: re-calculated at 340 nm(2) CP: OCRA/ROCINN-CRB	Daily GEOS-CF (0.25° × 0.25°)
	Fst_mler (Case F3)	LIDORT v3.6 (online)	Explicit	**KNMI TROPOMI v2.0 MLER at 340 nm**	CF: re-calculated at 340 nm(3) CP: OCRA/ROCINN-CRB	Daily GEOS-CF (0.25° × 0.25°)
	Fst_tm5 (Case F4)	LIDORT v3.6 (online)	Explicit	KNMI TROPOMI v2.0 DLER at 340 nm(1)	CF: calculated at 340 nm CP: OCRA/ROCINN-CRB	**Daily TM5-MP (1° × 1°)**

(1) KNMI TROPOMI v2.0 DLER at 340 nm over lands and coastal ocean regions, and MLER at 340 nm over open oceans.

(2) Fst_imaer (Case F2) cloud fraction is re-calculated with implicit aerosol corrections and different from that of Case F1.

(3) Fst_mler (Case F3) cloud fraction is re-calculated with KNMI TROPOMI v2.0 MLER and different from that of Case F1.

Species	Product or sensitivity test case	RT model	Aerosol correction	Surface reflectance	Cloud correction	A priori profiles
NO2	RPRO v2.4.0	DAK v3.2 (LUT)	Implicit	KNMI TROPOMI v1.0 DLER at 440 nm	CF: calculated at 440 nm CP: FRESCO-S	Daily TM5-MP (1° × 1°)
	POMINO (Case N0)	LIDORT v3.6 (online)	Explicit	MODIS MCD43C2.006 BRDF around 470 nm(4)	CF: re-calculated at 440 nm CP: FRESCO-S	Daily GEOS-CF (0.25° × 0.25°)
	Nst_imaer (Case N1)	LIDORT v3.6 (online)	**Implicit**	MODIS MCD43C2.006 BRDF around 470 nm(4)	CF: re-calculated at 440 nm(6) CP: FRESCO-S	Daily GEOS-CF (0.25° × 0.25°)
	Nst_dler (Case N2)	LIDORT v3.6 (online)	Explicit	**KNMI TROPOMI v2.0 DLER at 440 nm(5)**	CF: re-calculated at 440 nm(7) CP: FRESCO-S	Daily GEOS-CF (0.25° × 0.25°)
	Nst_tm5 (Case N3)	LIDORT v3.6 (online)	Explicit	MODIS MCD43C2.006 BRDF around 470 nm(4)	CF: re-calculated at 440 nm CP: FRESCO-S	**Daily TM5-MP (1° × 1°)**
	Nst_joint (Case N4)	LIDORT v3.6 (online)	**Implicit**	**KNMI TROPOMI v2.0 DLER at 440 nm(5)**	CF: re-calculated at 440 nm(8) CP: FRESCO-S	**Daily TM5-MP (1° × 1°)**

Atmospheric
Measurement
Techniques
Discussions
Open Access
EGU

(4) MODIS MCD43C2.006 BRDF around 470 nm over lands and coastal ocean regions, and KNMI TROPOMI v2.0 MLER at 440 nm over open oceans.

(5) KNMI TROPOMI v2.0 DLER at 440 nm over lands and coastal ocean regions, and MLER at 440 nm over open oceans.

(6) Nst_imaer (Case N1) cloud fraction is re-calculated with implicit aerosol corrections and different from that of Case N0.

(7) Nst_dler (Case N2) cloud fraction is re-calculated with KNMI TROPOMI v2.0 DLER and different from that of Case N0.

(8) Nst_joint (Case N4) cloud fraction is re-calculated with implicit aerosol corrections and KNMI TROPOMI v2.0 DLER, and different from that of Case N0.

216

2.3 Ground-based MAX-DOAS datasets

Ground-based MAX-DOAS instruments can provide vertical columns and profiles of trace gases from the surface up to the lower free troposphere (around 4 km). The measurement sensitivity is the highest near the surface and decreases at higher altitudes. Information on ground-based MAX-DOAS measurements used in this study is summarized in Table 2 with locations specified in Figure S2. For each site, we use Fiducial Reference Measurements for Ground-based DOAS Air-Quality Observations (FRM4DOAS; https://frm4doas.aeronomie.be/) version 01.01 harmonized HCHO and NO_2 data if available, otherwise we use data generated by principal investigators of each instrument using non-harmonized retrieval settings. The aim of the FRM4DOAS project is to minimize inhomogeneities in the current MAX-DOAS network to provide reference datasets for satellite data validation.

According to previous studies, the total estimated uncertainty of ground-based MAX-DOAS measurements in polluted conditions is about 30% for HCHO and NO_2 VCDs (De Smedt et al., 2021; Verhoelst et al., 2021). The mean bias is due mainly to systematic uncertainties related to AMF calculations. The uncertainty may also vary when different report strategies are used. Routine validation results show an overall bias of −37% for HCHO and −28% for NO_2 in the operational TROPOMI products compared to MAX-DOAS measurements in the validation report (available at https://mpc-vdaf.tropomi.eu/).

Table 2. MAX-DOAS datasets used for the validation. The sites are listed in the alphabetical order based on the first letter of the site name.

Station, country (lat/long)	Species	Owner/group	Retrieval type	Reference
Athens, Greece (38.05ºN, 23.86ºE)	NO_2	IUPB[1]	FRM4DOAS 01.01	https://frm4doas.aeronomie.be/
Bremen, German (53.10ºN, 8.85ºE)	HCHO and NO_2	IUPB	FRM4DOAS 01.01	https://frm4doas.aeronomie.be/
Cabauw, the Netherlands (51.97ºN, 4.93ºE)	HCHO and NO_2	KNMI[2]	FRM4DOAS 01.01	https://frm4doas.aeronomie.be/
Cape Hedo (26.87ºN, 128.25ºE)	NO_2	JAMSTEC[3]	Parameterized profiling (PP)	(Kanaya et al., 2014)
Chiba, Japan (35.63ºN, 140.10ºE)	NO_2	ChibaU[4]	Parameterized profiling (PP)	(Irie et al., 2011, 2012, 2015)
De Bilt, the Netherlands (52.10ºN, 5.18ºE)	HCHO and NO_2	KNMI	FRM4DOAS 01.01	https://frm4doas.aeronomie.be/
Fukue, Japan (32.75ºN, 128.68ºE)	NO_2	JAMSTEC	Parameterized profiling (PP)	(Kanaya et al., 2014)
Kinshasa, Democratic Republic of Congo (4.3ºS, 15.30ºE)	HCHO and NO_2	BIRA-IASB[5]	FRM4DOAS 01.01	https://frm4doas.aeronomie.be/

Mohali, India (30.67°N, 76.74°E)	HCHO and NO_2	IISER[6]/MPIC[7]	VCD from QA4ECV	(Kumar et al., 2020)
Xianghe, China (39.75°N, 116.96°E)	HCHO and NO_2	BIRA-IASB	FRM4DOAS 01.01	https://frm4doas.aeronomie.be/
Yokosuka, Japan (35.32°N, 139.65°E)	NO_2	JAMSTEC	Parameterized profiling (PP)	(Kanaya et al., 2014)

(1) Institute of Environmental Physics, University of Bremen
(2) Royal Netherlands Meteorological Institute
(3) Japan Agency for Marine-Earth Science and Technology
(4) Chiba University
(5) Royal Belgian Institute for Space Aeronomy
(6) Indian Institute of Science Education and Research
(7) Max Planck Institute for Chemistry

235

2.4 PGN/Pandora datasets

The Pandonia Global Network (PGN) is a large-scale global network providing ground-based observations of multiple atmospheric reactive trace gases, including HCHO and NO_2, and associated uncertainty values for satellite validation and other scientific activities. It is based on ground-based passive spectrometer systems called "Pandora" that can perform sun, moon and sky observations. The datasets have been widely used to validate HCHO and NO_2 measurements from satellite instruments and field campaigns (Herman et al., 2019; Kai-Sikhakhane et al., 2024; Li et al., 2021; Liu et al., 2024a; Verhoelst et al., 2021; Yombo Phaka et al., 2023). The nominal estimated uncertainty of total NO_2 columns is 0.27×10^{15} molec.cm^{-2} for the random part and 2.7×10^{15} molec.cm^{-2} for the systematic part, and an uncertainty of 20% is reported by comparisons with in-situ measurements (Verhoelst et al., 2021).

In this work, we only use HCHO and NO_2 direct sun total column measurements from the ESA Validation Data Centre (EVDC) (https://evdc.esa.int, last access: 17 July 2024). A total of 22 sites across the globe are selected for HCHO and NO_2 validation (Figure S2).

2.5 Data use and validation statistics

For comparison between satellite HCHO data, we filter out the retrieved data based on the following criteria: we exclude pixels with RPRO quality assurance values (QA) ≤ 0.5, which includes SZA or VZA > 70° or activated snow/ice flag. We also exclude pixels with POMINO-derived CRFs at 440 nm greater than 0.5, to minimize the impact of cloud contamination. The same criteria are applied to the NO_2 comparison as well. To examine the spatial distribution, gridded tropospheric HCHO and NO_2 VCDs in April, July, October 2021, and January 2022 at a resolution of 0.25° × 0.25° are calculated using an area-weighted oversampling technique (Zhang et al., 2023). For comparisons between satellite and ground-based HCHO data, we take two successive steps for data processing. First, we calculate the daily average HCHO columns from ground-based MAX-DOAS or PGN measurements within the time window between 11:00 and 16:00 LT. For PGN data, we only use those with the flag "assured high quality" or "not-assured high quality". Then we calculate daily average satellite HCHO columns based on pixels selected using the cloud information from POMINO retrieval, with the pixel center located within a radius of 20 km to the instruments. The daily collocated data pair is considered valid only if 10 satellite pixels or more are used for calculation. The processing for NO_2 data is different from that of HCHO in three aspects: (1) the time window for NO_2 is between 13:00 to 14:00 LT, as the diurnal variation of NO_2 is much stronger than that of HCHO;

264   (2) the radius between the satellite pixel center and the instrument is 5 km, considering the much larger spatial

265   gradient of the NO_2 distribution and less noise in the NO_2 retrieval; (3) we derive PGN tropospheric NO_2 columns

266   each day by subtracting stratospheric NO_2 columns from the RPRO NO_2 v2.4.0 L2 product over the instrument

267   from the total NO_2 columns, in order to make them comparable with satellite tropospheric NO_2 columns. Based

268   on collocated HCHO and NO_2 columns, we further compare the daily tropospheric column ratio of formaldehyde

269   to nitrogen dioxide (FNR) derived from satellite products and PGN measurements.

270   To quantify the performance of satellite products relative to ground-based measurements, we derive slope, offset

271   and correlation of the linear regression using the robust Theil-Sen estimator (Sen, 1968), which is insensitive to

272   occasional outliers. In a relative sense, we use normalized mean bias (NMB) to quantify the deviation between

273   satellite and ground-based measurements:

274
$$NMB = \frac{\overline{\Omega^{SAT}} - \overline{\Omega^{ground-based}}}{\overline{\Omega^{ground-based}}} \times 100\% \qquad (4)$$

275   with Ω being the HCHO or NO_2 vertical column in Sects. 6.1 and 6.2, and FNR in Sect. 6.3.

276   **3 Comparison of HCHO and NO_2 columns between POMINO and RPRO products**

277   Figures 1a and c illustrate the global distribution of tropospheric HCHO VCDs averaged over April, July, October

278   2021 and January 2022 from POMINO and RPRO retrieval, respectively. High levels of tropospheric HCHO

279   columns ($> 10 \times 10^{15}$ molec.cm^{-2}) are evident over the Amazonia Rainforest, Sub-Saharan Africa, South and East

280   Asia as well as North Australia. Enhanced HCHO concentrations are also noticeable in the southeastern United

281   States of America (USA) and Mexico, while localized hotspots with lower magnitudes are evident in the Middle

282   East and Europe. Over the remote background regions, HCHO is primarily from CH_4 oxidation, and the abundance

283   is about 3×10^{15} molec.cm^{-2} at maximum. Similarly, Figs. 1b and d show the POMINO and RPRO tropospheric

284   NO_2 VCDs in April, July, October 2021 and January 2022. High NO_2 columns are visible over three well-known

285   polluted regions, i.e., North China Plain, West Europe, and East USA, with strong hotspot signals over megacities

286   and metropolitan areas across the globe. Low NO_2 content in the remote atmosphere comes from aviation and

287   ship emissions, natural biogenic emissions, lightning and oxidation of long-lifetime species such as peroxyacetyl

288   nitrate (PAN).
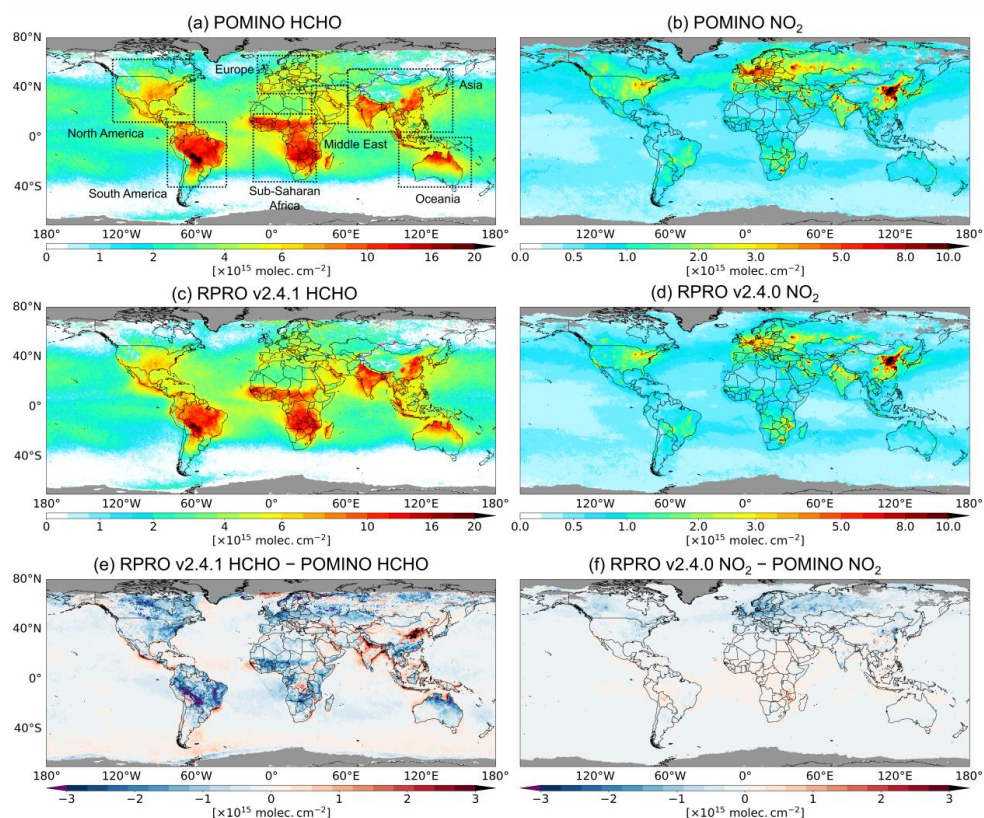
Figure 1. Spatial distribution of POMINO tropospheric HCHO and NO$_2$ VCDs (**a** and **b**), RPRO tropospheric HCHO and NO$_2$ VCDs (**c** and **d**), and respective absolute differences (**e** and **f**) at a spatial resolution of 0.25° × 0.25° averaged in April, July, October 2021, and January 2022. The black dashed rectangles illustrate the spatial range of the regions used for comparison. The regions in gray mean that there are no valid observations.

A high qualitative agreement is observed for both HCHO and NO$_2$ VCDs between RPRO and POMINO retrievals, as the same HCHO dSCDs and tropospheric NO$_2$ SCDs are used. However, as shown in Fig. 1e, RPRO HCHO tropospheric columns are lower by 2×10^{15} molec.cm^{-2} or more over almost all regions with elevated HCHO columns except North India and North China Plain; RPRO NO$_2$ columns are also lower than those of POMINO over most East China, India, Europe, and North America by up to about 20% in a relative sense, despite the positive differences over Sub-Saharan Africa and some cities such as Xi'an, Teheran, and Los Angeles (Fig. 1f). We further make the comparison in seven specific regions (bounded by black rectangles in Fig. 1a): North America (125°W-60°W, 10°N-65°N), South America (85°W-35°W, 40°S-10°N), Europe (10°W-35°E, 35°N-60°N), Sub-Saharan Africa (15°W-35°E, 35°S-20°N), Middle East (30°E-60°E, 10°N-40°N), Asia (60°E-145°E, 5°N-55°N), and Oceania (100°E-160°E, 40°S-0°). Figure 2 shows the comparison results over the most polluted areas in each region, defined as where the POMINO tropospheric HCHO or NO$_2$ VCDs averaged over April, July, October 2021 and January 2022 exceed their 99 percentiles; results for regional mean comparisons are shown in Figure S3. For HCHO, RPRO data are consistently lower than POMINO by around 15% over polluted areas in five regions, although the difference is small over the Middle East and Asia because of the cancellation between

308 positive and negative differences on the finer spatial scale. For NO_2, RPRO is smaller than POMINO by -19.4%

309 for North America and -23.3% for Europe. Detailed comparisons for each month are shown in Figure S4 and S5.

310 Overall, POMINO and RPRO HCHO and NO_2 retrievals show excellent agreement in a qualitative sense, but the

311 column values differ by 10% to 20% on average over polluted areas around the world. Such differences result

312 from the different cloud correction, aerosol correction, surface reflectance and vertical profile shapes used in AMF

313 calculations, which will be further discussed in Sect. 4.

314
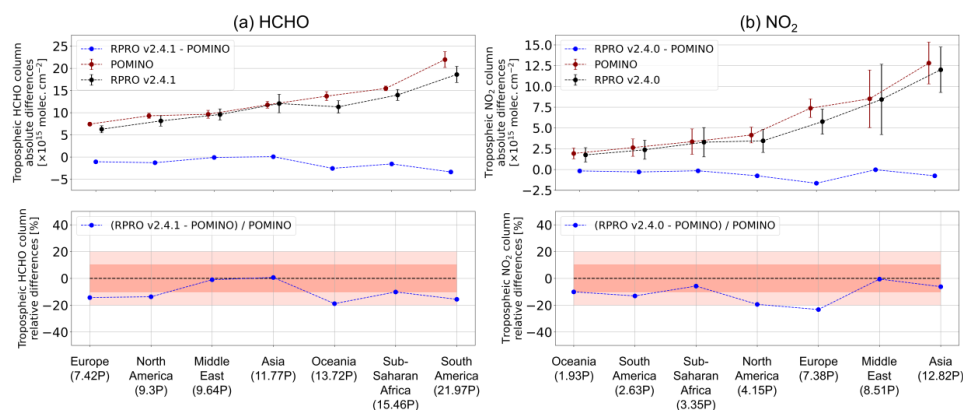
Figure 2. Absolute and relative differences between POMINO and RPRO (**a**) HCHO and (**b**) NO_2 tropospheric columns
averaged in April, July, October 2021, and January 2022 over polluted areas (defined as where POMINO mean HCHO or NO_2
columns exceed their 99 percentiles) in seven regions. Regions are sorted as a function of POMINO mean HCHO or NO_2
columns, with values (in the unit of "P" as $Pmolec.cm^{-2} = 1 \times 10^{15}$ $molec.cm^{-2}$) shown in the brackets in the bottom axis. Mean
POMINO (red) and RPRO (black) columns are also plotted with the absolute differences in the upper panel. Error bars
represent the standard deviations of the columns. Pink areas indicate 10% and 20% relative differences.

4 Sensitivity tests on AMF input parameters

322 As listed in Table 1, we implement a series of sensitivity tests to quantify the structural uncertainty from either

323 individual or joint effect of using different ancillary parameters in the HCHO and NO_2 AMF calculation. The time

324 period selected for the sensitivity analysis is July 2021 and January 2022, representing the summer and winter

325 time, respectively. Note that one of the most important features of the POMINO HCHO and NO_2 retrievals is that

326 they use the same cloud parameters for consistent cloud correction. Therefore, besides discussing the effect of

327 cloud correction based on POMINO cloud parameters, we also compare the differences between HCHO columns

328 retrieved using different cloud parameters, especially the cloud top pressures, which has never been discussed

329 before. The influences of aerosol correction, surface reflectance, a priori profile shapes and their joint effect are

330 discussed in the subsequent sub-sections.

4.1 Cloud correction

4.1.1 Effect of cloud correction based on POMINO cloud parameters

333 When calculating tropospheric AMFs, it is important to account for the influence of clouds on the radiative transfer

334 process in the atmosphere (Boersma et al., 2011; De Smedt et al., 2021; Lorente et al., 2017; Martin et al., 2002).

335 Clouds can either enhance or reduce the sensitivity to the trace gas molecules depending on their height relative

336 to the trace gas layers (the so-called "albedo" or "shielding" effect, respectively). Despite the relatively large

337 uncertainty of retrieved cloud parameters in near-cloud-free scenario (defined here as CF ≤ 0.1 or CRF ≤ 0.4)

338 (Richter and Burrows, 2002), most HCHO and NO_2 AMF algorithms make use of the IPA method (Sect. 2.1) to

339 explicitly account for the cloud effect.

340 Figure 3 shows the differences between clear-sky AMF and total AMF of all pixels with HCHO or NO_2 QA > 0.5

341 in July 2021 and January 2022, based on the FRESCO-S cloud top pressures and POMINO re-calculated cloud

342 fractions at 440 nm with explicit aerosol corrections. For both HCHO and NO_2, the differences between clear-sky

343 AMF and total AMF are negative when cloud top pressures are higher than 700 hPa, and their magnitudes continue

344 to increase along with the cloud top pressures. The negative differences can be as large as −30% for HCHO and

345 −20% for NO_2 when the CRFs are in the interval of 0.45 to 0.5 and cloud top pressures are higher than 900 hPa.

346 This illustrates the "albedo" effect of low clouds by increasing the contribution of photons from near-surface

347 layers to the ensemble of photons received at the satellite instrument and thus leading to higher total AMF.

348
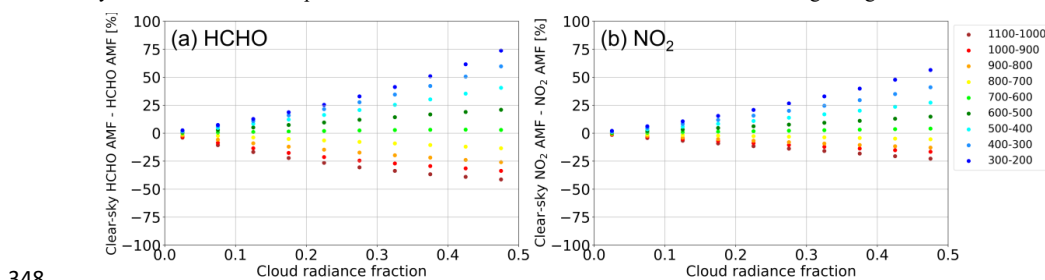
Figure 3. Differences of (**a**) HCHO and (**b**) NO_2 clear-sky AMF to total AMF for different cloud radiance fraction with an
interval of 0.05 in different cloud top pressure ranges (shown in different colors). All pixels with HCHO or NO_2 QA > 0.5 in
July 2021 and January 2022 are included.

352 On the contrary, clouds with cloud top pressure lower than 700 hPa reflect most photons back to the top of

353 atmosphere as a "shield" before they reach the HCHO or NO_2 abundant layers. As a result, positive differences of

354 clear-sky AMF to total AMF occur, and they increase as the cloud top pressures decrease, reaching 50% or more

355 when CRFs are in the interval of 0.4 to 0.5 and cloud top pressures are lower than 400 hPa. This result is also in

356 line with the previous study by Lorente et al. (2017).

357 In the global view (Figure 4), for both HCHO and NO_2 columns, the difference due to cloud correction (i.e., using

358 clear-sky AMF versus total AMF) is ±10% on average over high-value regions and can reach 40% over specific

359 areas. Note that all these comparisons are based on HCHO and NO_2 a priori profile shapes from GEOS-CF. The

360 signs and values of the differences might be different when using the profile shapes from another model, along

361 with the structural uncertainty discussed in Sect. 4.1.2.

Atmospheric
Measurement
Techniques
Discussions
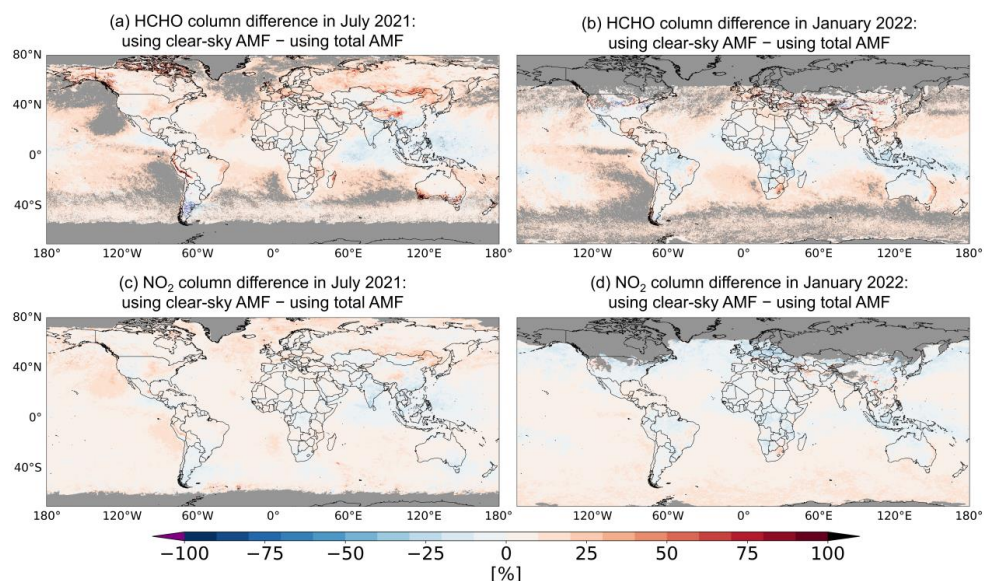
Figure 4. Relative differences of tropospheric HCHO (**a** and **b**) and NO$_2$ (**c** and **d**) columns derived using clear-sky POMINO AMF to those using total POMINO AMF in July 2021 and January 2022. The regions in gray mean that there are no valid observations.

4.1.2 Structural uncertainty of cloud correction based on different cloud parameters

The structural uncertainty of the cloud correction can be evaluated using cloud parameters from different cloud products. Lorente et al. (2017) have demonstrated that the systematic differences in cloud top pressure can lead to substantial differences in tropospheric NO$_2$ AMFs and VCDs. Focusing on HCHO in this section, we first compare the effective cloud fractions and cloud top pressures either calculated in different ways or from different products. As shown in the left column of Figure S6, POMINO-based ECF calculated at 440 nm and 340 nm as well as OCRA/ROCINN-CRB ECF show similar global patterns in July 2021. Despite the differences over certain areas, great agreement is exhibited between OCRA/ROCINN-CRB ECF and POMINO-based ECF calculated at 440 nm (linear regression slope of 0.92, offset of 0.02 and correlation coefficient of 0.80), and between POMINO-based ECF calculated at 340 nm and 440 nm (linear regression slope of 0.93, offset of 0.01 and correlation coefficient of 0.93). However, the OCRA/ROCINN-CRB cloud top pressures are significantly higher than those of the FRESCO-S product over the Amazonia Rainforest, Equatorial Africa and East China by 100-300 hPa, while the FRESCO-S cloud top pressures tend to be higher over many other places such as the Intertropical Convergence Zone (ITCZ) over the oceans (Fig. S6f). Such differences are systematic and are caused by different methodologies and ancillary parameters used in each cloud retrieval (Loyola et al., 2018; Van Geffen et al., 2022a), which are also reported in recent validation exercises using independent cloud measurements (Compernolle et al., 2021). As shown in Fig. 5, by comparing the result of POMINO to the test "Fst_ORcp" (Case F1, using the OCRA/ROCINN-CRB cloud top pressures and the POMINO-based ECFs calculated at 340 nm), we find differences of HCHO columns by up to 20% on average over highly polluted regions, as well as a positive increment over South America. Over remote background regions such as the Pacific Ocean, however, negative differences are found of 0.5-1 × 10^{15} molec.cm^{-2}. We attribute these differences to different OCRA/ROCINN-

387   CRB and FRESCO-S cloud top pressures, as ECFs in POMINO and Case "Fst_ORcp" are very close. Note that

388   this is a tentative estimate of HCHO column structural uncertainty from the choices of cloud parameters for cloud

389   correction, because the results are dependent on the explicit aerosol corrections and HCHO priori profile shapes

390   used in the tests.

391
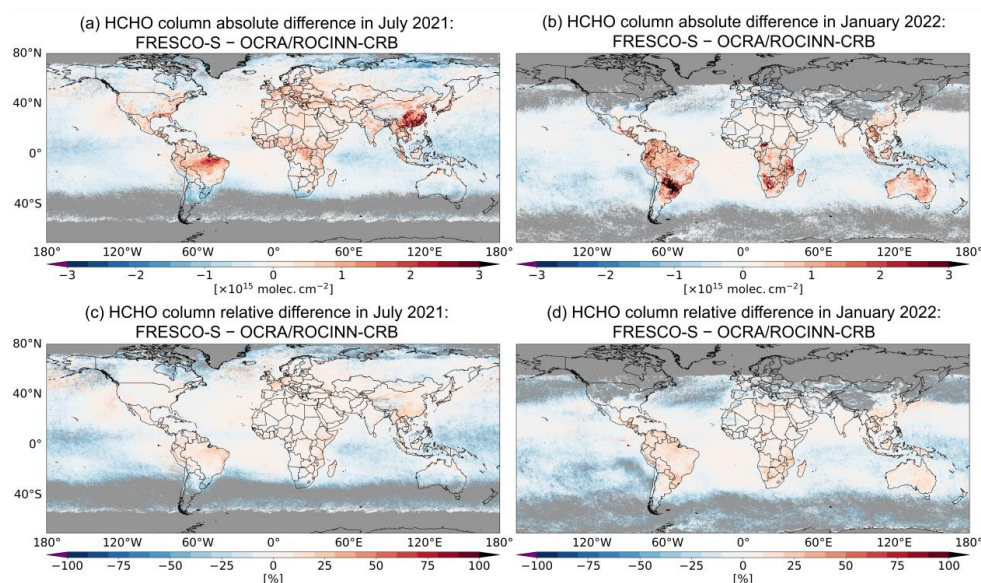
Figure 5. Absolute (first row) and relative differences (second row) of tropospheric HCHO columns of POMINO (using FRESCO-S cloud top pressures) to those of the sensitivity test "Fst_ORcp" (using OCRA/ROCINN-CRB cloud top pressures) in July 2021 and January 2022. Different cloud top pressures are emphasized in the title. The regions in gray mean that there are no valid observations.
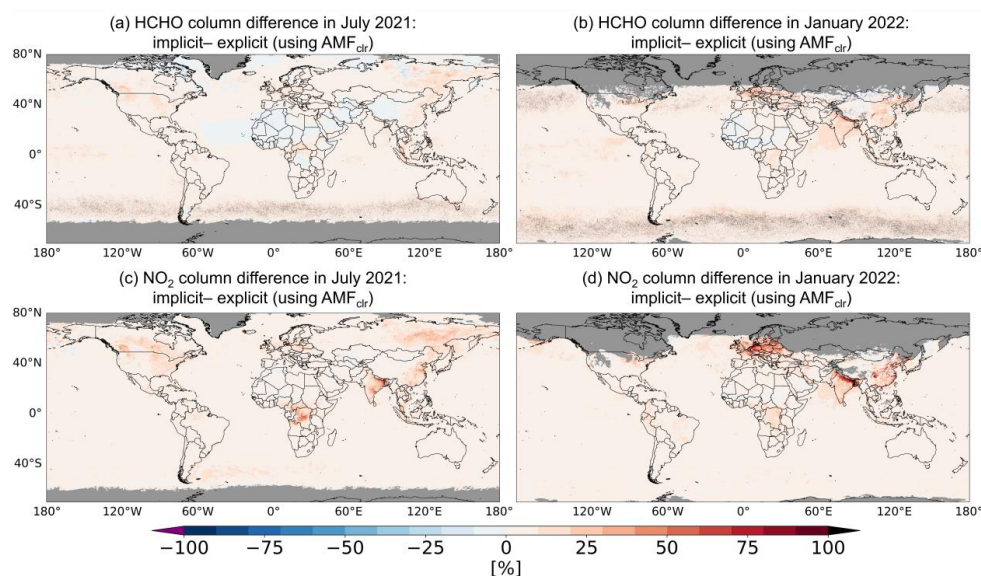
396   **4.2 Aerosol correction**

397   The influence of aerosols on AMF calculations is very complicated because they depend on the type of aerosols

398   (scattering or absorbing) and their height relative to the trace gases. The AMFs are generally increased when non-

399   absorbing aerosols are vertically collocated with or lower than the trace gases, while an opposite effect arises

400   when the non-absorbing aerosols reside vertically higher than the trace gases; On the other hand, absorbing

401   aerosols (e.g., black carbon) always reduce the sensitivity of the satellite instruments to the trace gases (Leitão et

402   al., 2010; Lin et al., 2014, 2015; Liu et al., 2024b). Figure S7 shows a global map of AOD at 340 nm and 440 nm

403   used in POMINO retrievals. Areas with heavy aerosol loads in July 2021 include North America, Equatorial Africa,

404   Middle East, India and East China due to biomass burning and/or anthropogenic activities; while in January 2022,

405   the aerosol content is significant in Equatorial Africa, North India and North China Plain. Different aerosol

406   corrections can directly change the clear-sky AMF, affect the retrieval of cloud information (cloud fraction in

407   particular) and modulate the AMF in the cloudy portion of the pixel. The latter two effects influence the total AMF

408   in an indirect way, and the impact on cloud information is often more significant than on cloudy-sky AMF

409   (Vasilkov et al., 2021).

410   Figure 6 shows that when using clear-sky AMFs to derive vertical columns, implicit aerosol corrections lead to

411   higher HCHO columns by 10% to 20 % over North America in July 2021, and the differences exceed 20% over

412   North India and East China in January 2022. A similar pattern is shown in the NO$_2$ comparison. This is because

413 when aerosols that reside vertically lower than or are mixed with HCHO and NO_2 molecules are excluded (i.e., in

414 the case of implicit corrections), the calculated AMFs are lower than those with explicit aerosol corrections. On

415 the other hand, for scenarios with strong anthropogenic emissions or biomass burning, where most HCHO and

416 NO_2 molecules are near the surface while aerosols reside above these trace gases, implicit aerosol corrections

417 neglect the strong "shielding" effect of the scattering aerosols and the strong absorption of photons by the

418 absorbing aerosols (e.g., BC), which leads to higher AMFs and lower vertical columns. The negative differences

419 of HCHO columns over the Democratic Republic of Congo in July 2021 (Fig. 6a) can be explained by the second
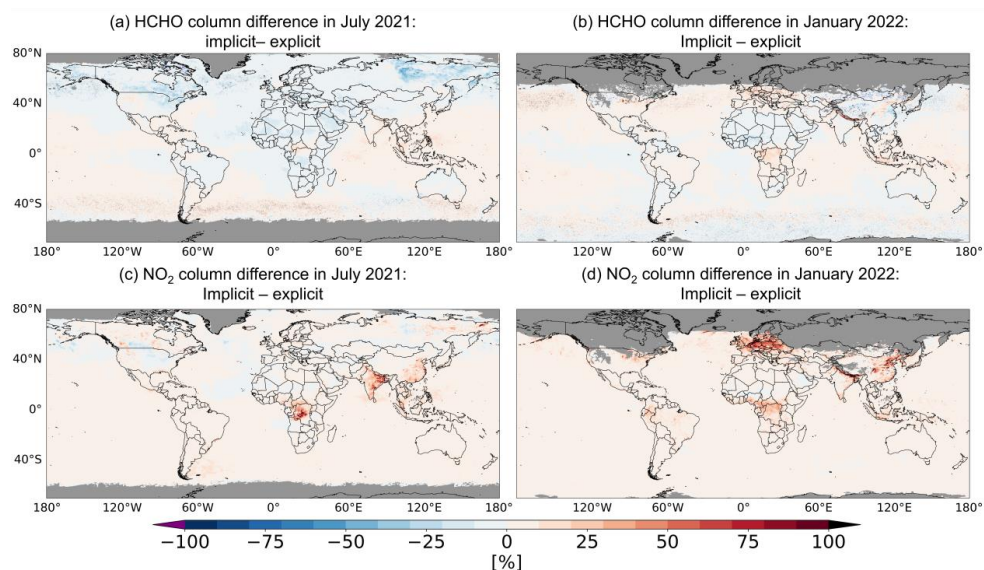
420 case.

Figure 6. Relative differences of tropospheric HCHO (**a** and **b**) and NO_2 (**c** and **d**) columns retrieved using clear-sky AMF with implicit aerosol corrections to those with explicit aerosol corrections in July 2021 and January 2022. The regions in gray mean that there are no valid observations.

425 For cloudy-sky AMF, the impact of non-absorbing aerosols above a cloud is negligible since we assume the cloud

426 to be an optically thick Lambertian reflectivity with a high albedo of 0.8 (Vasilkov et al., 2021). For absorbing

427 aerosols above the clouds, they can reduce the backscattered radiance and hence affect the cloudy-sky AMF.

428 However, Jethva et al. (2018) show that the occurrence of above-cloud absorbing aerosols is most frequent over

429 coastal and oceanic regions because of the long-range transport of aerosols and low-level stratocumulus clouds.

430 Over Southeast Asia during the springtime, the cloudy-sky frequency of occurrence of above-cloud absorbing

431 aerosols is 20% to 40%, probably caused by biomass burning activities. Retrievals under these conditions are

432 mostly discarded because the cloud fractions are too high to meet the filtering criteria for valid pixels (Sect. 2.5).

433 Therefore, the overall influence of implicit aerosol corrections on the cloud-sky AMF can be neglected and the

434 influence on the retrieval of cloud information, especially cloud fraction, is much more significant.

435 As explained in Sect. 2.2, explicit aerosol corrections affect the retrieved cloud (radiance) fraction due to the

436 inclusion of aerosol radiative contribution. This is also confirmed in Figure S8 that compares retrieved cloud

437 radiance fractions for the implicit versus explicit aerosol correction settings, in both UV and visible bands. As

438 shown in Figure 7, when using cloud-corrected AMFs to consider both direct and indirect aerosol optical effects

439 on the retrieval, the sign of HCHO relative differences over many regions is reversed from positive to negative

440 compared to Figs. 6a and b, such as North and South America. This reflects the enhanced cloud "albedo" effect

441 that increases the calculated HCHO scattering weights over the areas where cloud layers are vertically near or

442 below the HCHO layers. As for NO_2, similar results due to enhanced cloud "albedo" effect are found over North

443 America and East Russia in July 2021 (Fig. 7c), but the overall pattern in January 2022 remains the same as that

444 in Fig. 6d. Over the polluted regions in Asia and Europe, implicit aerosol corrections increase the retrieved NO_2

445 columns by 20% to 40% on average. This is because most NO_2 molecules over these polluted areas reside within

446 1 km above the ground and below the FRESCO-S cloud layers during wintertime, so the increased cloud fractions

447 due to implicit aerosol corrections enhance the "shielding" effect on tropospheric NO_2 AMF calculation and hence

448 higher NO_2 columns. The signs of the HCHO and NO_2 differences over North China Plain are not the same,

449 probably because of the differences between HCHO and NO_2 vertical profile shapes.

450

451 **Figure 7.** Relative differences of tropospheric HCHO (**a** and **b**) and NO_2 (**c** and **d**) columns retrieved using cloud-corrected
452 total AMF with implicit aerosol corrections (Cases "Fst_imaer" and "Nst_imaer") to those with explicit aerosol corrections
453 (Case "Fst_ORcp" and POMINO NO_2) in July 2021 and January 2022. The regions in gray mean that there are no valid
454 observations.

455 **4.3 Surface reflectance**

456 Compared to the LER model, which simply assumes the surface to be a Lambertian reflector, DLER partly

457 accounts for the anisotropy of the surface reflectance by building a certain relationship between the reflectance

458 and the satellite VZA, but its dependence on the SZA and RAA is still not included. The BRDF model fully

459 considers the surface optical property as a function of SZA, VZA, RAA and wavelength. At 340 nm, the

460 directionality of the surface reflectance is small over most regions (Kleipool et al., 2008). Figure S9 compares the

461 MODIS BRDF-derived blue-sky albedo (BSA, Schaepman-Strub et al., 2006) around 470 nm and KNMI

462 TROPOMI DLER at 440 nm over lands and coastal ocean regions. In both months, DLER shows higher values

463 than MODIS BSA except over desert and mountain regions, and the positive differences are larger than 0.1 over

Atmospheric
Measurement
Techniques
Discussions
Open Access

464 India in July 2021 and East Europe in January 2022. Reasons for these differences are not clear yet, but they are

465 likely associated with different parameters and corrections for aerosols and snow/ice cover in the algorithm.

466 Figures 8a and b present the influence of surface reflectance on HCHO retrievals. As it is well known that the

467 directionality of surface reflectance plays a marginal role in the retrieval based on the UV band, nearly no

468 difference is shown between HCHO columns retrieved using KNMI TROPOMI DLER and MLER at 340 nm.

469 However, the systematic differences between different MLER products are a more important source of the

470 structural uncertainty in HCHO AMFs. For example, KNMI TROPOMI MLER albedo at 340 nm is found to be

471 consistently lower than OMI climatology monthly MLER albedo used in the RPRO product by 0.01–0.05

472 (Kleipool et al., 2008; Tilstra et al., 2024).

473
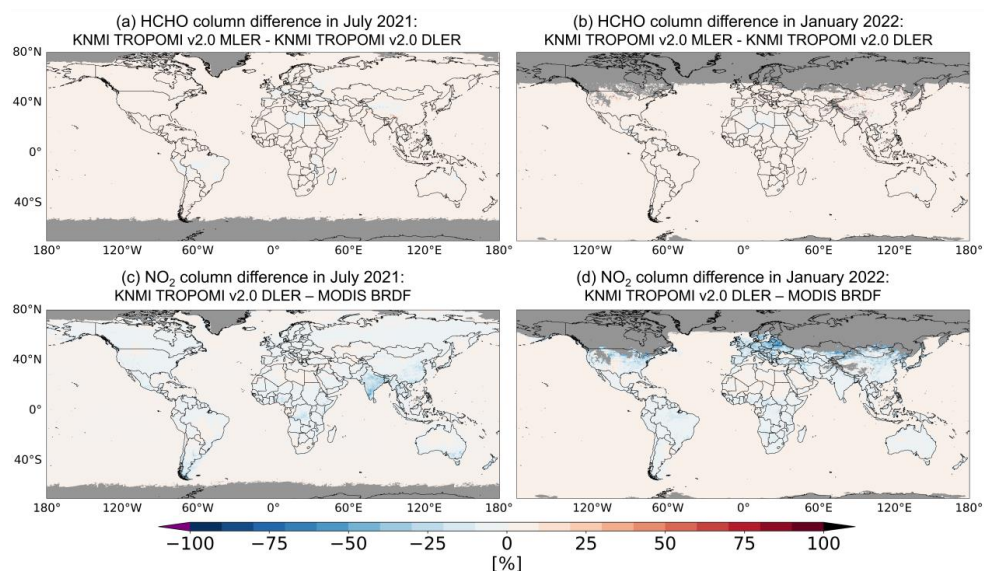
Figure 8. Relative differences of tropospheric HCHO columns retrieved using KNMI TROPOMI v2.0 MLER at 340 nm (Case
"Fst_mler") to those using KNMI TROPOMI v2.0 DLER at 340 nm (Case "Fst_ORcp") (**a** and **b**), and relative differences of
tropospheric NO_2 columns retrieved using KNMI TROPOMI v2.0 DLER at 440 nm (Case "Nst_dler") to those using MODIS
BRDF at 440 nm (POMINO NO_2) (**c** and **d**) in July 2021 and January 2022. The regions in gray mean that there are no valid
observations.

479 As for NO_2, Figs. 8c and d show significantly lower tropospheric NO_2 VCDs in the test "Nst_dler" (Case N2)

480 than those in the reference POMINO retrieval (Case N0) over most land areas. In January 2022, the NO_2 columns

481 retrieved using KNMI TROPOMI DLER are lower by 30% on average over the polluted regions with NO_2

482 columns larger than 10×10^{15} molec.cm^{-2} in Europe and North America. Like aerosols, the influence of surface

483 reflectance on AMFs is also a combination of the direct effect on clear-sky AMF and the indirect effect through

484 cloud correction (Boersma et al., 2011). As discussed by Tilstra (2024), DLER should not be considered as the

485 optimal replacement for the BRDF in the VIS wavelength. If the directional surface reflection can be modelled in

486 the RT calculation, it is better to use BRDF to derive surface reflectance for tropospheric NO_2 AMF calculation.

487 **4.4 A priori profiles**

488 In POMINO, we consistently use GEOS-CF HCHO and NO_2 vertical profile shapes as the prior information for

489 AMF calculations. Compared with TM5-MP model of which the spatial resolution is $1° \times 1°$, GEOS-CF features

Atmospheric
Measurement
Techniques
Discussions

490 a much finer spatial resolution (0.25º × 0.25º). The horizontal distributions of GEOS-CF and TM5-MP

491 tropospheric HCHO and NO_2 VCDs are shown in Figure S10, and comparisons of monthly mean HCHO and NO_2

492 vertical profiles between the models and the ground-based MAX-DOAS measurements are shown in Figure S11.

493 The differences between GEOS-CF, TM5-MP and MAX-DOAS profiles reflect the imperfections in these data

494 yet to be fully characterized (Keller et al., 2021; Williams et al., 2017), and they are also an important source of

495 structural uncertainty in HCHO and NO_2 retrievals.

496 Figure 9 shows the differences in retrieved HCHO and NO_2 VCDs caused by using different a priori vertical

497 profile shapes. The HCHO and NO_2 columns retrieved with TM5-MP prior information are obtained using AMFs

498 re-calculated by combining interpolated POMINO averaging kernels (AK) and TM5-MP a priori profile shapes.

499 As shown in Figs. 9a and b, the spatial patterns of HCHO relative differences are variable over different places

500 and in different months, and are generally more significant than the individual effects of clouds, aerosols and

501 surface reflectance changes (Figs. 4, 7 and 8). At the regional level, the HCHO structural uncertainty from a priori

502 profile shapes is 20% to 30% over the background clean areas, and 10% to 20% over the polluted areas. In contrast,

503 the NO_2 differences caused by different a priori profile shapes are around 10% over the clean areas and reach 30%

504 or more over the polluted areas. Over East China, India and the Middle East, localized differences over cities and

505 polluted regions are obvious (Figs. 9c and d), reflecting the significant differences between TM5-MP and GEOS-

506 CF NO_2 profile shapes. Besides, distinctive patterns along the coastal lines are visible, especially in the HCHO

507 relative differences. This is caused by the relatively coarse horizontal resolution of TM5-MP, in which the large

508 heterogeneity of HCHO vertical distribution is smoothed in the 1º × 1º grid.
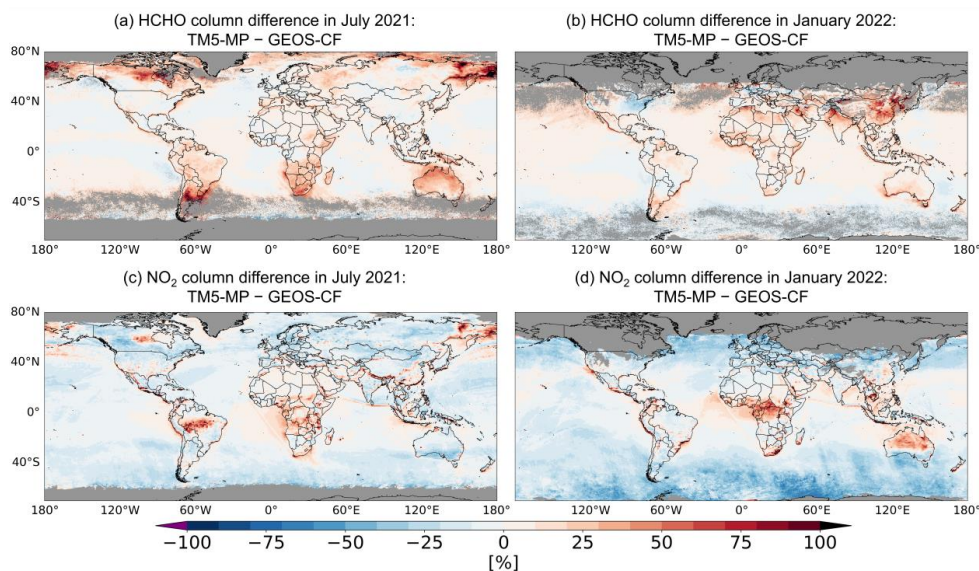
Figure 9. Relative differences of tropospheric HCHO (**a** and **b**) and NO_2 (**c** and **d**) columns retrieved with TM5-MP priori profiles (Cases "Fst_tm5" and "Nst_tm5") to those with GEOS-CF priori profiles (Case "Fst_ORcp" and POMINO NO_2) in July 2021 and January 2022. The regions in gray mean that there are no valid observations.

4.5 Summarizing the impacts of input parameters

514 As shown in each sub-figure of Figure 10, the first three columns summarize the structural uncertainty of aerosol

515 correction, surface reflectance and a priori profile shapes on the HCHO retrieval in the corresponding region and

516 month. As noted in Sect. 2.2, we consistently use GEOS-CF HCHO columns for background correction in every

517 HCHO sensitivity test case. The TM5-MP HCHO columns over background regions are systematically lower than

518 those of GEOS-CF by about 0.5×10^{15} molec.cm^{-2} on average (Fig. S10), which strongly affects the comparisons

519 over the low-HCHO regions.

520 Over clean areas (HCHO columns $< 5 \times 10^{15}$ molec.cm^{-2}), a priori profile shapes are the primary source of the

521 HCHO structural uncertainty (third column in Fig. 10). However, the differences between "Fst_tm5" and the

522 reference case "Fst_ORcp" are not in alignment with those of RPRO to the reference case, as manifested in the

523 consistent drop of the blue line from the third ("Fst_tm5" – reference) to the fourth column (RPRO − reference).

524 This drop can be attributed to the systematic issue in the background correction. Over most areas with HCHO

525 columns larger than 5×10^{15} molec.cm^{-2}, relative to the same reference case, the HCHO differences caused by

526 using implicit aerosol corrections and TM5-MP priori profile shapes match well with those of RPRO product (the

527 fourth column). However, the lower values of RPRO than the reference case in Europe in January 2022 do not

528 agree with the combined results of tests "Fst_imaer" and "Fst_tm5". This indicates that the higher OMI-based

529 climatology monthly MLER used in RPRO retrieval is probably the dominant factor. Furthermore, the influence

530 of cloud correction using different cloud parameters, especially the cloud top pressures, varies from −20% to 20%

531 depending on the specific regions and seasons. This is also an important factor for the HCHO differences between

532 POMINO and RPRO retrievals.

Atmospheric
Measurement
Techniques
Open Access
Discussions

EGU

533
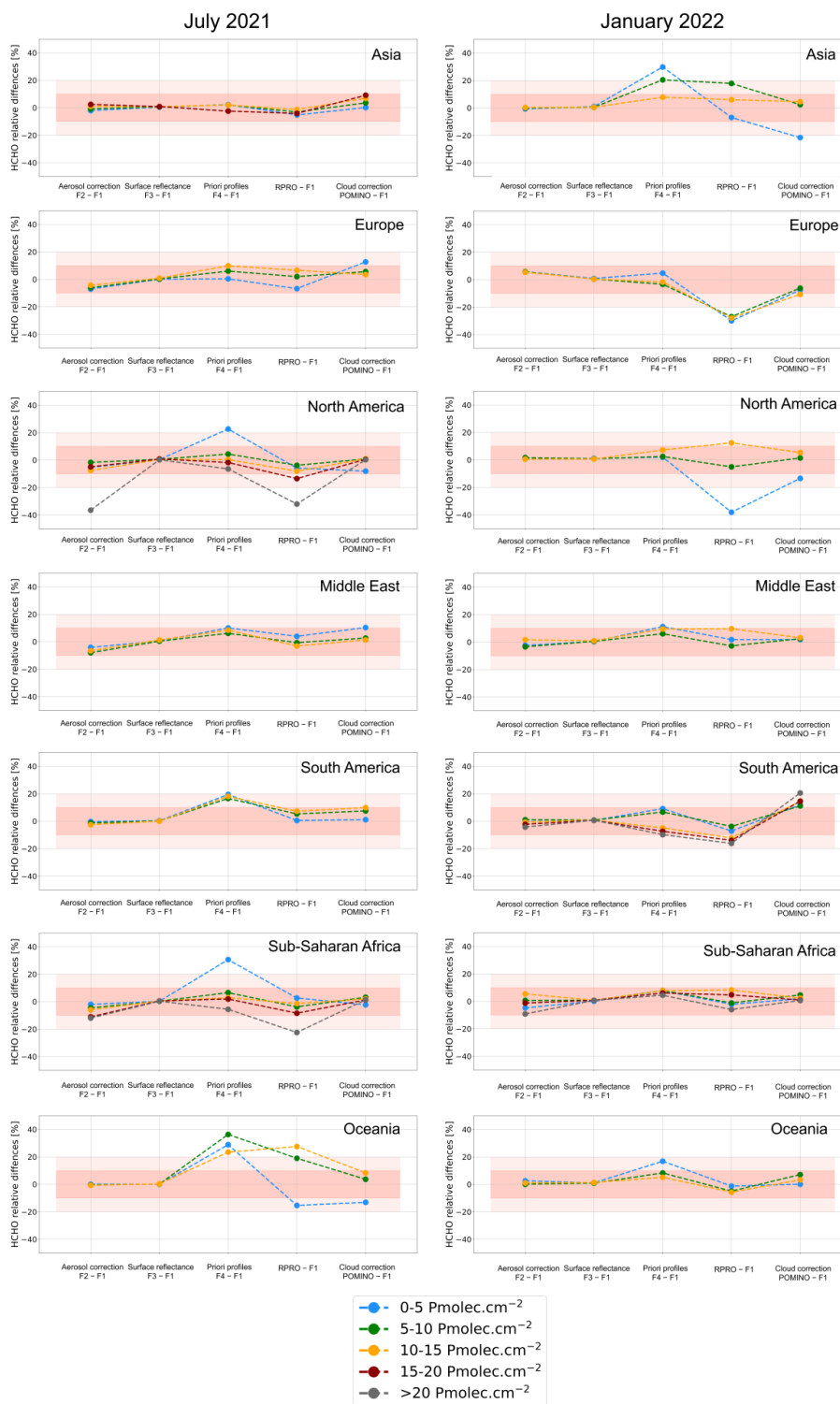
Figure 10. HCHO relative differences of the sensitivity test "Fst_imaer" (Case F2, first column), "Fst_mler" (Case F3, second column), "Fst_tm5" (Case F4, third column), RPRO product (fourth column) and POMINO product (fifth column) to the reference "Fst_ORcp" (Case F1) over seven regions in July 2021 and January 2022.

537

538   For NO_2, the first three columns in Figure 11 show the individual effect of each input parameter on the NO_2

539   retrieval in each region. Apparently, the relative differences between RPRO and POMINO (the fifth column) are

540   in discrepancy with the sum of the differences between each of the three cases ("Nst_imaer", "Nst_dler" and

541   "Nst_tm5") and the reference POMINO retrieval, especially over polluted areas in North America, Europe and

542   Asia in January 2022. However, the NO_2 columns of the test "Nst_joint" (Case N4) show high agreement with

543   those of the RPRO product when compared to the POMINO retrieval (fourth column in Fig. 11); a similar result

544   is shown for the spatial distribution in Figure S12. Therefore, the NO_2 differences between POMINO and RPRO

545   are the result of compensation effects between different aerosol corrections on one hand, and different surface

546   reflectances as well as vertical profile shapes on the other hand. These results demonstrate the non-linear joint

547   effects of aerosols, surface reflectance, clouds and a priori profiles in the AMF calculation, which are consistent

548   with the previous findings (Lin et al., 2015; Liu et al., 2020). The remaining differences between "Nst_joint" and

549   RPRO NO_2 columns are caused by their different ways to obtain tropospheric NO_2 AMFs, i.e., online pixel-

550   specific RT calculation versus LUT-based interpolation (Lin et al., 2014).

Atmospheric
Measurement
Techniques
Open Access

EGU

Discussions
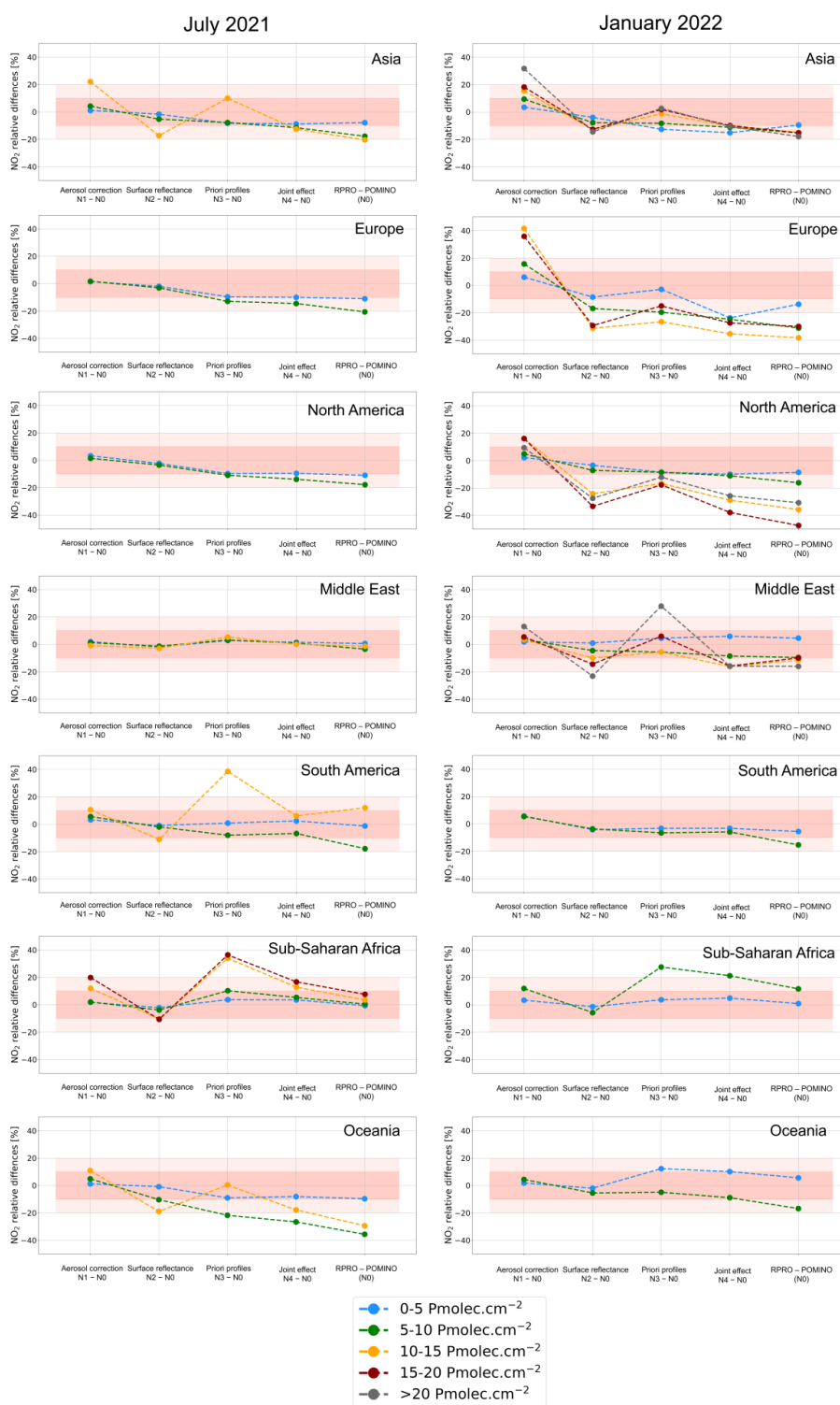
Figure 11. NO$_2$ relative differences of the sensitivity test "Nst_imaer" (Case N1, first column), "Nst_dler" (Case N2, second column), "Nst_tm5" (Case N3, third column), "Nst_joint" (Case N4, fourth column) and RPRO product (fifth column) to POMINO product as the reference (Case N0) over seven regions in July 2021 and January 2022.

5 Uncertainty estimates

The theoretical uncertainties of the POMINO retrievals can be analytically derived by uncertainty propagation based on the Eqs. 2 and 3 (Boersma et al., 2004). However, it is difficult to estimate the overall AMF uncertainty for each pixel, as one challenge is the amount of computational costs of sensitivity calculations with the online pixel-by-pixel RT simulations. Nonetheless, random uncertainties of the observations can be reduced by spatial and temporal averaging, although the systematic uncertainties from the main retrieval steps remain. There remains lack of information to separate random and systematic uncertainties accurately. Here we provide a preliminary estimate of the uncertainty budget for monthly averaged HCHO and NO$_2$ columns from POMINO retrievals, based on our sensitivity tests and validations as well as previous work.

For HCHO, the contribution from the slant column uncertainty to the vertical column uncertainty is 25% for regions with low columns and 15% for regions with elevated columns (De Smedt, 2022; De Smedt et al., 2018). The contribution from the background correction uncertainty is significant for low columns (around 40%), in which the systematic uncertainty from the dSCD normalization is estimated to be 0 to 4×10^{15} molec.cm^{-2}, and the uncertainty from the model background is 0 to 2×10^{15} molec.cm^{-2}. The AMF uncertainty, which is the largest contributor to the vertical column uncertainty, is mainly dependent on the errors of the ancillary parameters tested in Sect. 4. The AMF uncertainty induced by the error of a priori profile shapes is the largest with 30% to 60% over clean regions and around 20% over polluted regions. The errors of cloud parameters and surface reflectance are assumed to contribute to the AMF uncertainty by 10% to 20%, and the errors in the aerosol parameters contribute to the AMF uncertainty by about 5% for regions with low columns and 10% for regions with elevated columns. Overall, the HCHO AMF uncertainty is estimated to be about 50% for clean regions and 30% for polluted regions, respectively.

For NO$_2$, the total SCD uncertainty is reported to be 0.5 to 0.6×10^{15} molec.cm^{-2} and a constant value of 0.2×10^{15} molec.cm^{-2} is assigned to the uncertainty of the stratospheric SCDs (Van Geffen et al., 2022b). For tropospheric AMF, the uncertainty caused by aerosol-related errors is estimated to be 10% to 20% on average, and the errors in a priori NO$_2$ profile shapes is estimated to cause an AMF uncertainty of 20% based on the sensitivity test. The contribution from cloud parameters and surface reflectance to the NO$_2$ AMF uncertainty is estimated to be on the same level as that to the HCHO AMF uncertainty discussed above. By adding these errors in quadrature, the overall NO$_2$ AMF uncertainty is 10% to 20% for clean regions and 20% to 30% for polluted regions.

By wrapping up the estimated relative contributions to the vertical column uncertainty, the total uncertainty of POMINO HCHO VCDs is estimated to be 50% to 70% over regions with low columns, and 30% to 40% over regions with high columns. For the POMINO NO$_2$ retrieval, the total uncertainty is around 50% over remote regions with low NO$_2$ abundances, and 20% to 30% over polluted regions with high NO$_2$ abundances. This tentative estimation of the POMINO retrieval uncertainties is supported by the validation results against the independent ground-based measurements (Sect. 6.1). To quantify the errors for individual pixels, artificial-intelligence-based methods are an appealing approach to be tried in our future work.
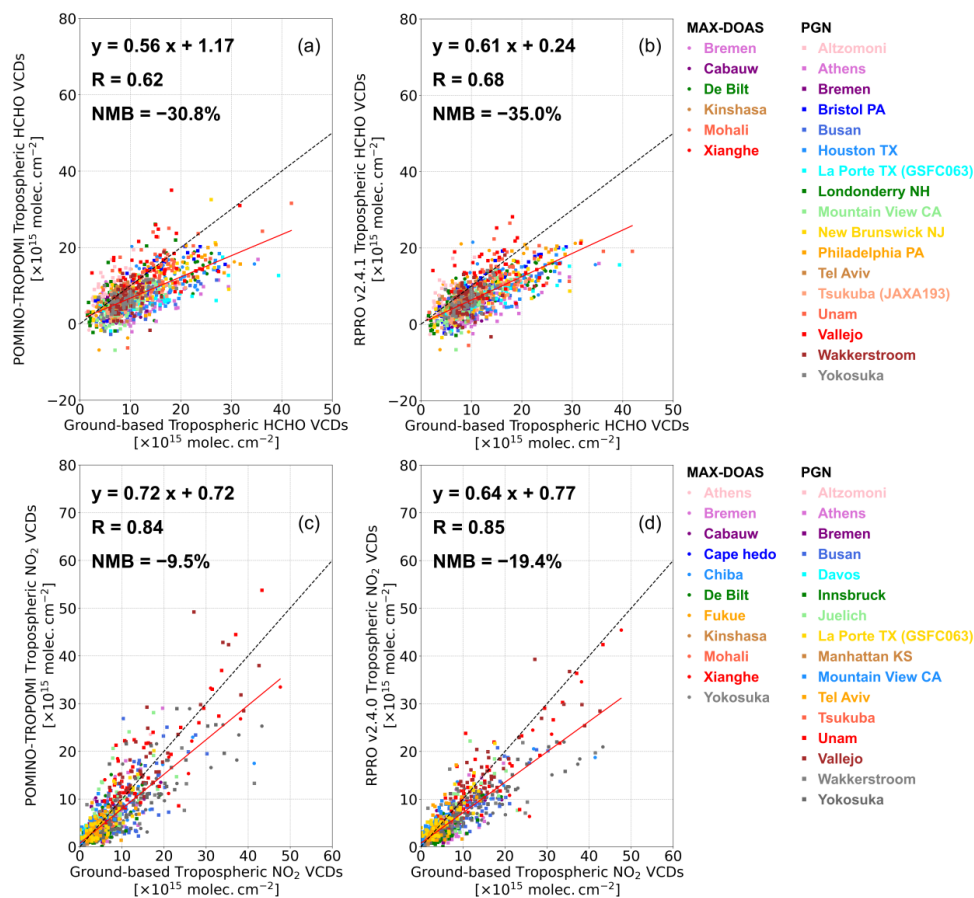
Atmospheric
Measurement
Techniques
Discussions

6 Validation against global MAX-DOAS network and PGN measurements

In this section, we present the validation results of POMINO and RPRO retrievals against independent ground-based measurements from the global MAX-DOAS network and PGN. Separate comparisons of tropospheric HCHO and NO_2 columns are given in Sect. 6.1, the effect of vertical smoothing is discussed in Sect. 6.2, and the satellite-based and ground-based FNRs are evaluated in Sect. 6.3.

6.1 Validation of tropospheric HCHO and NO_2 columns

Figures 12a and b present the scatterplots of daily satellite HCHO columns against ground-based measurements in April, July, October 2021 and January 2022. Each data point represents a day and site. There is a lower slope and higher positive offset for POMINO compared with those of RPRO product (slope: 0.56 versus 0.61; offset: 1.17 versus 0.24). This is in line with the discussion in Sect. 4.5 that POMINO employs higher HCHO columns from GEOS-CF for background correction, which is the major component of HCHO columns over areas with low HCHO level. Furthermore, at 13 polluted ground-based sites where HCHO columns are higher than 10×10^{15} molec.cm^{-2}, POMINO HCHO columns show smaller bias at 8 sites (Figure S13). Overall, POMINO exhibits a smaller negative NNB (-30.8%) than RPRO (-35.0%). Statistics of separate validation results against MAX-DOAS and PGN measurements are given in Table S2.

Atmospheric
Measurement
Techniques

Discussions

Figure 12. Scatterplots of tropospheric HCHO (**a** and **b**) and NO$_2$ (**c** and **d**) columns between satellite products (POMINO and RPRO) and ground-based measurements in April, July, October 2021 and January 2022. The slope, offset and correlation from a linear regression using the robust Theil-Sen estimator and normalized mean bias (NMB) are given in each panel and plotted as the red line. The black dashed line is the 1:1 line. Each MAX-DOAS (marked by circles) and PGN site (marked by squares) is color-coded and listed on the right side.

For NO$_2$, a better agreement with ground-based measurements is found for POMINO tropospheric columns than for RPRO (slope: 0.72 versus 0.64; offset: 0.72 versus 0.77; NMB: −9.5% versus −19.4%). At remote MAX-DOAS sites where tropospheric NO$_2$ columns are around 1×10^{15} molec.cm^{-2} or less (Fig. S13), satellite tropospheric NO$_2$ columns are higher by $0.3\text{-}1 \times 10^{15}$ molec.cm^{-2}. This is in line with the previous validation studies (Kanaya et al., 2014; Verhoelst et al., 2021; Zhang et al., 2023), and is probably because that a majority of NO$_2$ molecules over remote regions are in the free troposphere, which are above the detection height of ground-based MAX-DOAS instruments but can be well observed by spaceborne instruments. At the six most-polluted sites with mean tropospheric NO$_2$ columns higher than 10×10^{15} molec.cm^{-2}, POMINO features a much-reduced bias of −14.5% compared with RPRO product (−22.0%). This is because of the explicit correction for aerosol "shielding" effect over highly polluted sites and lower surface reflectance, which reduces the NO$_2$ scattering weights near the surface and hence increases the retrieved NO$_2$ columns.

6.2 Effect of vertical smoothing for validation

To test the impact of different vertical sensitivity from the ground and space, MAX-DOAS FRM$_4$DOAS v01.01 harmonized HCHO and NO$_2$ datasets were used. The data provides 20-layer-resolved (from surface to ~ 600 hPa) MAX-DOAS averaging kernels and vertical profiles (posterior and prior to the retrievals). Following the "vertical smoothing" technique (Rodgers and Connor, 2003) described in detail by Vigouroux et al. (2020), we first substituted the priori profile shapes used in MAX-DOAS retrieval with either GEOS-CF or TM5-MP profile shapes to get corrected MAX-DOAS retrieved profiles:

$$x'_{\mathrm{MD}} = x_{\mathrm{MD}} + (\mathbf{A}_{\mathrm{MD}} - \mathbf{I})(x_{\mathrm{MD,a}} - x_{\mathrm{Sat,a}}) \tag{5}$$

with x'_{MD} denoting the corrected MAX-DOAS retrieved profile, x_{MD} the original MAX-DOAS profile, $\mathbf{A}_{\mathrm{MD}}$ the MAX-DOAS averaging kernel matrix, $\mathbf{I}$ the unit matrix, $x_{\mathrm{MD,a}}$ the MAX-DOAS a priori profile and $x_{\mathrm{Sat,a}}$ the satellite a priori profile (i.e., from GEOS-CF or TM5-MP) re-gridded to the MAX-DOAS retrieval resolution from the surface to 600 hPa. To account for the trace gas content in the free troposphere, especially for HCHO, we further extend the corrected MAX-DOAS profile to the tropopause with the satellite profile above 600 hPa that is scaled to ensure vertical continuity of the overall tropospheric profile. After that, we perform the smoothing process using either POMINO or RPRO averaging kernels:

$$c_{\mathrm{MD}}^{\mathrm{smoothed}} = a_{\mathrm{Sat}} \cdot x'_{\mathrm{MD}} \tag{6}$$

with $c_{\mathrm{MD}}^{\mathrm{smoothed}}$ the smoothed MAX-DOAS column, a_{Sat} the satellite averaging kernel vector and x'_{MD} the corrected MAX-DOAS retrieved profile from Eq. (5). We compare the smoothed MAX-DOAS data with satellite retrievals and the statistics are summarized in Table 3.

For the five MAX-DOAS sites available (Table 2), we find that after smoothing, the linear regression slope gets improved for both HCHO products. The negative bias of POMINO is reduced by about 10% but that of RPRO product is increased by about 4%. This is because POMINO HCHO averaging kernels are smaller than those of RPRO between the surface to about 800 hPa, resulting in lower smoothed MAX-DOAS HCHO columns compared to those using RPRO HCHO averaging kernels. Smaller POMINO HCHO averaging kernels at low altitudes are due to enhanced "shielding" effect from explicit aerosol corrections and lower KNMI TROPOMI MLER than OMI-based climatological monthly MLER used in RPRO HCHO.

For NO$_2$, among the six sites (Table 2), after applying the vertical smoothing technique, the negative NMB increases from −7.3% to −15.7% for POMINO and decreases from −24.6% to −8.5% for RPRO, even though a better day-to-day correlation is found for both products. Again, such changes are caused by the different averaging kernels used in the two satellite products.

Due to the scarcity of the MAX-DOAS sites for analysis here (Tables 2 and 3) and the under-representativeness in their spatial distribution (Table 2), a general conclusion cannot be made on the overall impact of vertical smoothing now. Nevertheless, the comparison results indicate the importance of considering the different vertical sensitivity between spaceborne and ground-based MAX-DOAS instruments, and different a priori profile shapes used to derive the vertical columns during the validation practice (De Smedt et al., 2021; Dimitropoulou et al., 2022; Yombo Phaka et al., 2023).

Table 3. Effect of vertical smoothing on the comparisons of TROPOMI and MAX-DOAS data.

HCHO (five sites)	Direct comparisons		Vertical smoothing applied	
	POMINO	RPRO	POMINO	RPRO
Slope	0.56	0.65	1.08	0.72

Offset [10^{15} molec.cm^{-2}]	2.15	0.18	−1.58	−0.78
Correlation	0.63	0.66	0.66	0.73
NMB	−22.6%	−30.8%	−10.9%	−34.2%

NO$_2$ (six sites)	Direct comparisons		Vertical smoothing applied	
	POMINO	RPRO	POMINO	RPRO
Slope	0.80	0.64	0.72	0.74
Offset [10^{15} molec.cm^{-2}]	0.38	0.46	0.74	0.98
Correlation	0.81	0.84	0.90	0.86
NMB	−7.3%	−24.6%	−15.7%	−8.5%

659

6.3 Comparisons of FNR

661   The FNR is an important space-based indicator of the ozone chemistry regimes and its sensitivity to precursor
662   emissions. Figure 13 shows the scatterplots of daily FNR derived from POMINO and RPRO products against
663   PGN measurements in April, July, October 2021 and January 2022. A better agreement is found between POMINO
664   and PGN FNR with improved linear regression statistics (slope: 0.72 versus 0.67; offset: 0.15 versus 0.21; R: 0.83
665   versus 0.82) and reduced NMB (−18.4% versus −24.1%) compared to those of RPRO products. Moreover, the
666   regression results are better in the comparisons for FNR than those in the individual comparisons for either HCHO
667   or NO$_2$ tropospheric VCDs (Sect. 6.1). This demonstrates the potential of using POMINO HCHO and NO$_2$
668   retrievals to improve the studies on the ozone sensitivity analysis for NO$_x$ as well as VOC emission controls.

669
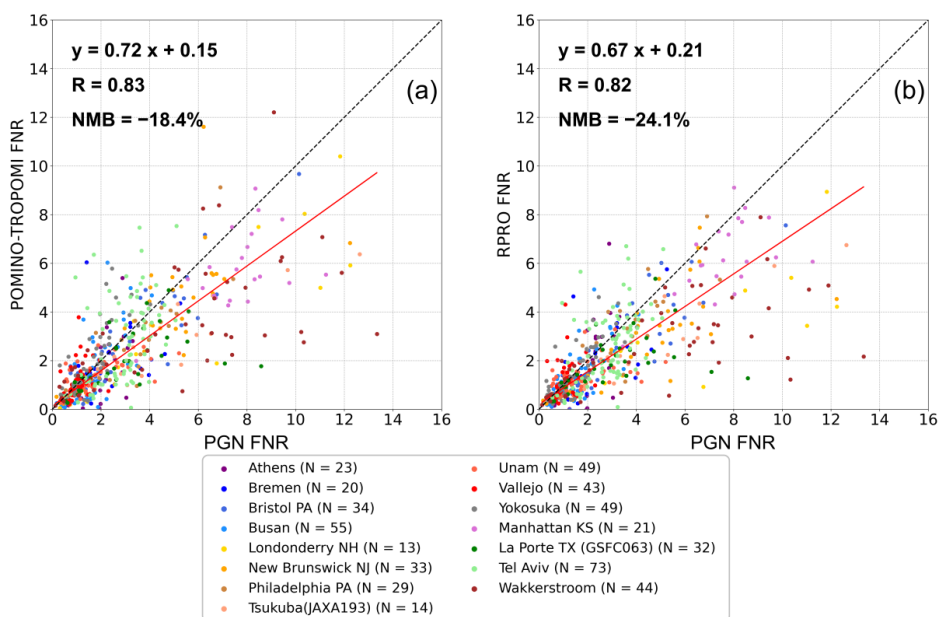
Figure 13. Scatterplots of daily tropospheric column ratio of formaldehyde to nitrogen dioxide (FNR) derived from satellite
products (**a** for POMINO and **b** for RPRO) and PGN measurements in April, July, October 2021 and January 2022. The slope,
offset and correlation from a linear regression using the robust Theil-Sen estimator and normalized mean bias (NMB) are given
in each panel and plotted as the red line.

674   Note that more than half of the PGN stations used here are in the North America (Figure S2), thus further validation

675   with ground-based measurements in combination with model simulations is needed over other regions, especially

676   those where ozone chemistry regimes change rapidly.

677   **7 Conclusions**

678   We developed an updated version of the POMINO algorithm providing HCHO and NO_2 AMF calculations, which

679   offers global tropospheric HCHO and NO_2 VCDs retrievals of TROPOMI with improved consistency compared

680   to current products. Compared to the independently developed RPRO HCHO and NO_2 operational algorithms

681   using different ancillary parameters, the POMINO algorithm includes: (1) the surface reflectance anisotropy by

682   using KNMI TROPOMI v2.0 DLER at 340 nm for HCHO and MODIS BRDF coefficients around 470 nm for

683   NO_2, (2) an explicit aerosol correction for both species based on GEOS-CF aerosol information and MODIS AOD

684   at corresponding wavelengths, (3) high-resolution ($0.25º \times 0.25º$) a priori HCHO and NO_2 profile shapes from

685   GEOS-CF dataset and (4) a consistent cloud correction based on cloud top pressures taken from the FRESCO-S

686   cloud product and cloud fractions re-calculated at 440 nm using the same ancillary parameters as those used in

687   NO_2 AMF calculation.

688   High qualitative agreement of tropospheric HCHO and NO_2 columns is found between POMINO and RPRO

689   products in April, July, October 2021 and January 2022. However, RPRO HCHO columns are lower by 15% on

690   average than the POMINO HCHO columns over the polluted areas around the world, and the negative differences

691   of RPRO tropospheric NO_2 columns can reach −20% over specific areas.

692   To clarify the reasons for the differences between POMINO and RPRO columns and quantify the structural

693   uncertainty from ancillary parameters in the AMF calculation, we performed a series of sensitivity tests on the

694   cloud correction, aerosol correction, surface reflectance and a priori profile shapes. We find that based on

695   POMINO-recalculated cloud fraction at 440 nm and FRESCO-S cloud top pressures, differences between clear-

696   sky AMFs and total AMFs vary from −25% to more than 50% for both HCHO and NO_2, depending on the cloud

697   fraction and the relative height between clouds and trace gases. When using cloud top pressure data from

698   OCRA/ROCINN-CRB instead of FRESCO-S, a large decrease of tropospheric HCHO columns is found ($> 2 \times$

699   10^{15} molec.cm^{-2}) over Amazonia Rainforest and southeast China, and the negative differences over polluted

700   regions are about 20% on average.

701   The influence of the implicit aerosol corrections used in operational products is within 10% on the HCHO retrieval,

702   while higher NO_2 columns by 20% to 40% over the polluted areas in January 2022 are found with implicit aerosol

703   corrections. Comparisons of retrieved NO_2 columns using clear-sky AMFs and total AMFs with implicit aerosol

704   corrections prove that the positive difference for NO_2 is dominated by the enhanced "shielding" effect of clouds

705   over NO_2 layers. The directionality of the surface reflectance has a very small impact on the HCHO retrieval in

706   the UV band, but the structural uncertainty of surface reflectance for NO_2 over polluted areas can reach 30%. The

707   HCHO structural uncertainty from a priori profile shapes is 20% to 30% over the background areas and 10% to

708   20% over the polluted areas. In contrast, the NO_2 differences due to different a priori profile shapes reach 30% or

709   more over the polluted areas. The additional test on the joint effect of these parameters shows notable non-linear

710   influences from aerosol correction, surface reflectance, cloud correction and a priori profile shapes in the RT

711   calculation.

712 Direct comparisons of tropospheric HCHO and NO_2 columns between satellite retrievals and ground-based
713 measurements from the global MAX-DOAS network and PGN show that both POMINO HCHO and NO_2
714 retrievals feature a reduced bias in comparison to RPRO products (HCHO: -30.8% versus -35.0%; NO_2: -9.5%
715 versus -19.4%), especially at the polluted sites. The effect of the vertical smoothing is significant and strongly
716 depends on the satellite averaging kernels. A better agreement of daily FNR with smaller bias is also found
717 between POMINO products and PGN measurements in comparison to results obtained with RPRO products ($R =$
718 0.83, NMB $= -18.4\%$ versus $R = 0.82$, NMB $= -24.1\%$).

719 Overall, we demonstrate the promising performance of TROPOMI-based POMINO algorithm for global HCHO
720 and NO_2 retrieval. However, there are still several limitations in our study. First, in the process of cloud correction
721 in the POMINO retrieval, only the cloud fraction is re-calculated with explicit aerosol corrections, while the cloud
722 top pressure is taken from the external dataset, i.e., the FRESCO-S cloud product, in which the aerosols are
723 implicitly accounted for (at least partly). Therefore, this step leads to a potential double counting of aerosols in
724 the cloud information, as discussed in detail in Liu et al. (2020). Given that TROPOMI-based O_2-O_2 cloud data
725 have become available, we plan to improve the current POMINO algorithm by performing O_2-O_2 cloud retrieval
726 for both cloud fraction and cloud top pressure with explicit aerosol corrections in the future, as has been done in
727 the POMINO-OMI and POMINO-GEMS products (Lin et al., 2015; Liu et al., 2019; Zhang et al., 2023).

728 Second, it should be noted that the indirect aerosol effect on HCHO and NO_2 retrievals through clouds is strongly
729 sensitive to the cloud top pressures and the trace gas profile shapes. Using OMI O_2-O_2 based cloud parameters or
730 FRESCO-S cloud top pressures stored in the operational NO_2 L2 product before version 1.4.0, previous studies
731 have shown lower NO_2 columns over polluted North China Plain when retrieved with implicit aerosol corrections
732 (Lin et al., 2015; Liu et al., 2020). This is because the cloud top pressures in those studies are higher, which result
733 in larger AMF values when implicit (instead of explicit) aerosol corrections are used. Besides, certain biases still
734 exist in the current FRESCO-S cloud top pressures, such as the overestimation over the ITCZ. The effect of a
735 priori profile shapes is also significant for both HCHO and NO_2 retrievals, and it deserves more attention in the
736 future analysis. Comprehensive evaluations of cloud retrievals and model performance with independent
737 measurements are needed in future studies.

738 Nevertheless, the POMINO algorithm that aims at improving the consistency in multi-gas retrieval shows great
739 potential and can be easily adapted to other satellite instruments, e.g. GEMS, the Tropospheric Emissions:
740 Monitoring Pollution (TEMPO), as well as Sentinel-4 and Sentinel-5 missions. The global tropospheric HCHO
741 and NO_2 VCD retrievals presented in our study are also of value for subsequent applications such as ozone
742 chemistry analysis and emission controls.

743

744 *Data availability.* The POMINO HCHO and NO_2 datasets presented in the study will be available soon on our
745 website (http://www.pku-atmos-acm.org/acmProduct.php/). The S5p TROPOMI RPRO HCHO v2.4.1 L2 product
746 and RPRO NO_2 v2.4.0 L2 product are available at Copernicus Data Space Ecosystem | Europe's eyes on Earth
747 (https://dataspace.copernicus.eu/, last access: 17 July 2024). The ground-based MAX-DOAS measurements can
748 be provided upon request to the corresponding authors. The PGN/Pandora direct sun measurements are available
749 at the ESA Validation Data Centre (EVDC, 2024) (https://evdc.esa.int, last access: 7 July 2024) and Pandonia
750 Global Network (2024) (https://www.pandonia-global-network.org/, last access: 17 July 2024).

751

752   *Supplement.*

753

754   *Author contributions.* YZ, JL, NT and MVL conceived this research. YZ, HY, IDS, JL, NT and MVL designed

755   the algorithm. YZ, HY, IDS, JL, MVL, GP, AM and SC designed the validation process together. YZ performed

756   all calculations. RS provided LIDORT model. RN, FR, SW, LC, JVG, ML, WS and LF provided data and technical

757   support for satellite retrievals. GP and SC provided methodological support for validation. AMC is the network

758   principal investigator (PI) for PGN/Pandora instruments. MVL, GP, AM, MMF, AR, AP, VK, VS, TW, YC, HT,

759   YK and HI provided ground-based MAX-DOAS measurements. YZ wrote the paper with inputs from JL, NT,

760   IDS and MVR. All co-authors revised and commented on the paper.

761

762   *Competing interests.* At least one of the (co-)authors is a member of the editorial board of Atmospheric

763   Measurement Techniques. The authors have no other competing interests to declare.

764

774   **References**

775   Beelen, R., Stafoggia, M., Raaschou-Nielsen, O., Andersen, Z. J., Xun, W. W., Katsouyanni, K.,

776   Dimakopoulou, K., Brunekreef, B., Weinmayr, G., Hoffmann, B., Wolf, K., Samoli, E., Houthuijs,

777   D., Nieuwenhuijsen, M., Oudin, A., Forsberg, B., Olsson, D., Salomaa, V., Lanki, T., Yli-Tuomi, T.,

778   Oftedal, B., Aamodt, G., Nafstad, P., De Faire, U., Pedersen, N. L., Östenson, C.-G., Fratiglioni, L.,

779   Penell, J., Korek, M., Pyko, A., Eriksen, K. T., Tjønneland, A., Becker, T., Eeftens, M., Bots, M.,

780   Meliefste, K., Wang, M., Bueno-de-Mesquita, B., Sugiri, D., Krämer, U., Heinrich, J., de Hoogh, K.,

781   Key, T., Peters, A., Cyrys, J., Concin, H., Nagel, G., Ineichen, A., Schaffner, E., Probst-Hensch, N.,

782   Dratva, J., Ducret-Stich, R., Vilier, A., Clavel-Chapelon, F., Stempfelet, M., Grioni, S., Krogh, V.,

783   Tsai, M.-Y., Marcon, A., Ricceri, F., Sacerdote, C., Galassi, C., Migliore, E., Ranzi, A., Cesaroni, G.,

784   Badaloni, C., Forastiere, F., Tamayo, I., Amiano, P., Dorronsoro, M., Katsoulis, M., Trichopoulou,

785   A., Vineis, P., and Hoek, G.: Long-term Exposure to Air Pollution and Cardiovascular Mortality: An

786   Analysis of 22 European Cohorts, Epidemiology, 25, 368,

787   https://doi.org/10.1097/EDE.0000000000000076, 2014.

788 Boersma, K. F., Eskes, H. J., and Brinksma, E. J.: Error analysis for tropospheric NO2 retrieval from
789   space, AGU J., 2004.

790 Boersma, K. F., Eskes, H. J., Dirksen, R. J., van der A, R. J., Veefkind, J. P., Stammes, P., Huijnen, V.,
791   Kleipool, Q. L., Sneep, M., Claas, J., Leitão, J., Richter, A., Zhou, Y., and Brunner, D.: An improved
792   tropospheric NO_2 column retrieval algorithm for the Ozone Monitoring Instrument, Atmospheric
793   Meas. Tech., 4, 1905–1928, https://doi.org/10.5194/amt-4-1905-2011, 2011.

794 Bovensmann, H., Burrows, J. P., Buchwitz, M., Frerick, J., Noël, S., Rozanov, V. V., Chance, K. V.,
795   and Goede, A. P. H.: SCIAMACHY: Mission Objectives and Measurement Modes, 1999.

796 Burrows, J. P., Weber, M., Buchwitz, M., Rozanov, V., Ladstätter-Weißenmayer, A., Richter, A.,
797   DeBeek, R., Hoogen, R., Bramstedt, K., Eichmann, K.-U., Eisinger, M., and Perner, D.: The Global
798   Ozone Monitoring Experiment (GOME): Mission Concept and First Scientific Results, 1999.

799 Callies, J., Corpaccioli, E., Eisinger, M., Hahne, A., and Lefebvre, A.: GOME-2 – Metop's Second-
800   Generation Sensor for Operational Ozone Monitoring, 2000.

801 Chen, L., Lin, J., Martin, R., Du, M., Weng, H., Kong, H., Ni, R., Meng, J., Zhang, Y., Zhang, L., and
802   van Donkelaar, A.: Inequality in historical transboundary anthropogenic PM2.5 health impacts, Sci.
803   Bull., 67, 437–444, https://doi.org/10.1016/j.scib.2021.11.007, 2022.

804 Compernolle, S., Argyrouli, A., Lutz, R., Sneep, M., Lambert, J.-C., Fjæraa, A. M., Hubert, D., Keppens,
805   A., Loyola, D., O'Connor, E., Romahn, F., Stammes, P., Verhoelst, T., and Wang, P.: Validation of
806   the Sentinel-5 Precursor TROPOMI cloud data with Cloudnet, Aura OMI O_2–O_2, MODIS, and Suomi-
807   NPP VIIRS, Atmospheric Meas. Tech., 14, 2451–2476, https://doi.org/10.5194/amt-14-2451-2021,
808   2021.

809 Cooper, M. J., Martin, R. V., Hammer, M. S., Levelt, P. F., Veefkind, P., Lamsal, L. N., Krotkov, N.
810   A., Brook, J. R., and McLinden, C. A.: Global fine-scale changes in ambient NO2 during COVID-19
811   lockdowns, Nature, 601, 380–387, https://doi.org/10.1038/s41586-021-04229-0, 2022.

812 Crutzen, P. J.: The influence of nitrogen oxides on the atmospheric ozone content, Q. J. R. Meteorol.
813   Soc., 96, 320–325, https://doi.org/10.1002/qj.49709640815, 1970.

814 De Smedt, I.: TROPOMI ATBD of HCHO data products version 2.4.1, 2022.

815 De Smedt, I., Stavrakou, T., Müller, J.-F., van der A, R. J., and Van Roozendael, M.: Trend detection
816   in satellite observations of formaldehyde tropospheric columns, Geophys. Res. Lett., 37,
817   https://doi.org/10.1029/2010GL044245, 2010.

818 De Smedt, I., Theys, N., Yu, H., Danckaert, T., Lerot, C., Compernolle, S., Van Roozendael, M., Richter,
819   A., Hilboll, A., Peters, E., Pedergnana, M., Loyola, D., Beirle, S., Wagner, T., Eskes, H., van Geffen,
820   J., Boersma, K. F., and Veefkind, P.: Algorithm theoretical baseline for formaldehyde retrievals from
821   S5P TROPOMI and from the QA4ECV project, Atmospheric Meas. Tech., 11, 2395–2426,
822   https://doi.org/10.5194/amt-11-2395-2018, 2018.

823 De Smedt, I., Pinardi, G., Vigouroux, C., Compernolle, S., Bais, A., Benavent, N., Boersma, F., Chan,
824   K.-L., Donner, S., Eichmann, K.-U., Hedelt, P., Hendrick, F., Irie, H., Kumar, V., Lambert, J.-C.,

825   Langerock, B., Lerot, C., Liu, C., Loyola, D., Piters, A., Richter, A., Rivera Cárdenas, C., Romahn,
826   F., Ryan, R. G., Sinha, V., Theys, N., Vlietinck, J., Wagner, T., Wang, T., Yu, H., and Van Roozendael,
827   M.: Comparative assessment of TROPOMI and OMI formaldehyde observations and validation
828   against MAX-DOAS network column measurements, Atmospheric Chem. Phys., 21, 12561–12593,
829   https://doi.org/10.5194/acp-21-12561-2021, 2021.

830   Dimitropoulou, E., Hendrick, F., Friedrich, M. M., Tack, F., Pinardi, G., Merlaud, A., Fayt, C., Hermans,
831   C., Fierens, F., and Van Roozendael, M.: Horizontal distribution of tropospheric NO_2 and aerosols
832   derived by dual-scan multi-wavelength multi-axis differential optical absorption spectroscopy (MAX-
833   DOAS) measurements in Uccle, Belgium, Atmospheric Meas. Tech., 15, 4503–4529,
834   https://doi.org/10.5194/amt-15-4503-2022, 2022.

835   Herman, J., Abuhassan, N., Kim, J., Kim, J., Dubey, M., Raponi, M., and Tzortziou, M.:
836   Underestimation of column NO_2 amounts from the OMI satellite compared to diurnally varying
837   ground-based retrievals from multiple PANDORA spectrometer instruments, Atmospheric Meas.
838   Tech., 12, 5593–5612, https://doi.org/10.5194/amt-12-5593-2019, 2019.

839   Irie, H., Takashima, H., Kanaya, Y., Boersma, K. F., Gast, L., Wittrock, F., Brunner, D., Zhou, Y., and
840   Van Roozendael, M.: Eight-component retrievals from ground-based MAX-DOAS observations,
841   Atmospheric Meas. Tech., 4, 1027–1044, https://doi.org/10.5194/amt-4-1027-2011, 2011.

842   Irie, H., Boersma, K. F., Kanaya, Y., Takashima, H., Pan, X., and Wang, Z. F.: Quantitative bias
843   estimates for tropospheric NO_2 columns retrieved from SCIAMACHY, OMI, and GOME-2 using a
844   common   standard   for   East   Asia,   Atmospheric   Meas.   Tech.,   5,   2403–2411,
845   https://doi.org/10.5194/amt-5-2403-2012, 2012.

846   Irie, H., Nakayama, T., Shimizu, A., Yamazaki, A., Nagai, T., Uchiyama, A., Zaizen, Y., Kagamitani,
847   S., and Matsumi, Y.: Evaluation of MAX-DOAS aerosol retrievals by coincident observations using
848   CRDS, lidar, and sky radiometer inTsukuba, Japan, Atmospheric Meas. Tech., 8, 2775–2788,
849   https://doi.org/10.5194/amt-8-2775-2015, 2015.

850   Jethva, H., Torres, O., and Ahn, C.: A 12-year long global record of optical depth of absorbing aerosols
851   above the clouds derived from the OMI/OMACA algorithm, Atmospheric Meas. Tech., 11, 5837–
852   5864, https://doi.org/10.5194/amt-11-5837-2018, 2018.

853   Jiang, Z., Zhu, R., Miyazaki, K., McDonald, B. C., Klimont, Z., Zheng, B., Boersma, K. F., Zhang, Q.,
854   Worden, H., Worden, J. R., Henze, D. K., Jones, D. B. A., Denier van der Gon, H. A. C., and Eskes,
855   H.: Decadal Variabilities in Tropospheric Nitrogen Oxides Over United States, Europe, and China, J.
856   Geophys. Res. Atmospheres, 127, e2021JD035872, https://doi.org/10.1029/2021JD035872, 2022.

857   Jin, X. and Holloway, T.: Spatial and temporal variability of ozone sensitivity over China observed
858   from the Ozone Monitoring Instrument, J. Geophys. Res. Atmospheres, 120, 7229–7246,
859   https://doi.org/10.1002/2015JD023250, 2015.

860   Jin, X., Fiore, A. M., Murray, L. T., Valin, L. C., Lamsal, L. N., Duncan, B., Folkert Boersma, K., De
861   Smedt, I., Abad, G. G., Chance, K., and Tonnesen, G. S.: Evaluating a Space-Based Indicator of

862   Surface Ozone-NO-VOC Sensitivity Over Midlatitude Source Regions and Application to Decadal

863   Trends, J. Geophys. Res. Atmospheres, 122, 10,439-10,461, https://doi.org/10.1002/2017JD026720,

864   2017.

865   Jin, X., Fiore, A., Boersma, K. F., Smedt, I. D., and Valin, L.: Inferring Changes in Summertime Surface

866   Ozone–NOx–VOC Chemistry over U.S. Urban Areas from Two Decades of Satellite and Ground-

867   Based Observations, Environ. Sci. Technol., 54, 6518–6529, https://doi.org/10.1021/acs.est.9b07785,

868   2020.

869   Jin, X., Fiore, A. M., and Cohen, R. C.: Space-Based Observations of Ozone Precursors within

870   California Wildfire Plumes and the Impacts on Ozone-NOx-VOC Chemistry, Environ. Sci. Technol.,

871   57, 14648–14660, https://doi.org/10.1021/acs.est.3c04411, 2023.

872   Kai-Sikhakhane, R. F., Scholes, M. C., Piketh, S. J., van Geffen, J., Garland, R. M., Havenga, H., and

873   Scholes, R. J.: Assessing Nitrogen Dioxide in the Highveld Troposphere: Pandora Insights and

874   TROPOMI Sentinel-5P Evaluation, Atmosphere, 15, 1187, https://doi.org/10.3390/atmos15101187,

875   2024.

876   Kanaya, Y., Irie, H., Takashima, H., Iwabuchi, H., Akimoto, H., Sudo, K., Gu, M., Chong, J., Kim, Y.

877   J., Lee, H., Li, A., Si, F., Xu, J., Xie, P.-H., Liu, W.-Q., Dzhola, A., Postylyakov, O., Ivanov, V.,

878   Grechko, E., Terpugova, S., and Panchenko, M.: Long-term MAX-DOAS network observations of

879   NO_2 in Russia and Asia (MADRAS) during the period 2007–2012: instrumentation,

880   elucidation of climatology, and comparisons with OMI satellite observations and global model

881   simulations, Atmospheric Chem. Phys., 14, 7909–7927, https://doi.org/10.5194/acp-14-7909-2014,

882   2014.

883   Keller, C. A., Knowland, K. E., Duncan, B. N., Liu, J., Anderson, D. C., Das, S., Lucchesi, R. A.,

884   Lundgren, E. W., Nicely, J. M., Nielsen, E., Ott, L. E., Saunders, E., Strode, S. A., Wales, P. A., Jacob,

885   D. J., and Pawson, S.: Description of the NASA GEOS Composition Forecast Modeling System

886   GEOS-CF   v1.0,   J.   Adv.   Model.   Earth   Syst.,   13,   e2020MS002413,

887   https://doi.org/10.1029/2020MS002413, 2021.

888   Kim, J., Jeong, U., Ahn, M.-H., Kim, J. H., Park, R. J., Lee, H., Song, C. H., Choi, Y.-S., Lee, K.-H.,

889   Yoo, J.-M., Jeong, M.-J., Park, S. K., Lee, K.-M., Song, C.-K., Kim, S.-W., Kim, Y. J., Kim, S.-W.,

890   Kim, M., Go, S., Liu, X., Chance, K., Miller, C. C., Al-Saadi, J., Veihelmann, B., Bhartia, P. K.,

891   Torres, O., Abad, G. G., Haffner, D. P., Ko, D. H., Lee, S. H., Woo, J.-H., Chong, H., Park, S. S.,

892   Nicks, D., Choi, W. J., Moon, K.-J., Cho, A., Yoon, J., Kim, S., Hong, H., Lee, K., Lee, H., Lee, S.,

893   Choi, M., Veefkind, P., Levelt, P. F., Edwards, D. P., Kang, M., Eo, M., Bak, J., Baek, K., Kwon, H.-

894   A., Yang, J., Park, J., Han, K. M., Kim, B.-R., Shin, H.-W., Choi, H., Lee, E., Chong, J., Cha, Y., Koo,

895   J.-H., Irie, H., Hayashida, S., Kasai, Y., Kanaya, Y., Liu, C., Lin, J., Crawford, J. H., Carmichael, G.

896   R., Newchurch, M. J., Lefer, B. L., Herman, J. R., Swap, R. J., Lau, A. K. H., Kurosu, T. P., Jaross,

897   G., Ahlers, B., Dobber, M., McElroy, C. T., and Choi, Y.: New Era of Air Quality Monitoring from

898   Space: Geostationary   Environment   Monitoring   Spectrometer   (GEMS),

899   https://doi.org/10.1175/BAMS-D-18-0013.1, 2020.

900   Kleipool, Q. L., Dobber, M. R., de Haan, J. F., and Levelt, P. F.: Earth surface reflectance climatology

901   from 3 years of OMI data, J. Geophys. Res. Atmospheres, 113, https://doi.org/10.1029/2008JD010290,

902   2008.

903   Kong, H., Lin, J., Chen, L., Zhang, Y., Yan, Y., Liu, M., Ni, R., Liu, Z., and Weng, H.: Considerable

904   Unaccounted Local Sources of NOx Emissions in China Revealed from Satellite, Environ. Sci.

905   Technol., 56, 7131–7142, https://doi.org/10.1021/acs.est.1c07723, 2022.

906   Kumar, V., Beirle, S., Dörner, S., Mishra, A. K., Donner, S., Wang, Y., Sinha, V., and Wagner, T.:

907   Long-term MAX-DOAS measurements of NO_2, HCHO, and aerosols and evaluation of corresponding

908   satellite data products over Mohali in the Indo-Gangetic Plain, Atmospheric Chem. Phys., 20, 14183–

909   14235, https://doi.org/10.5194/acp-20-14183-2020, 2020.

910   Leitão, J., Richter, A., Vrekoussis, M., Kokhanovsky, A., Zhang, Q. J., Beekmann, M., and Burrows, J.

911   P.: On the improvement of NO_2 satellite retrievals – aerosol impact on the airmass factors,

912   Atmospheric Meas. Tech., 3, 475–493, https://doi.org/10.5194/amt-3-475-2010, 2010.

913   Levelt, P. F., van den Oord, G. H. J., Dobber, M. R., Malkki, A., Visser, H., Vries, J. de, Stammes, P.,

914   Lundell, J. O. V., and Saari, H.: The ozone monitoring instrument, IEEE Trans. Geosci. Remote Sens.,

915   44, 1093–1101, https://doi.org/10.1109/TGRS.2006.872333, 2006.

916   Li, J., Wang, Y., Zhang, R., Smeltzer, C., Weinheimer, A., Herman, J., Boersma, K. F., Celarier, E. A.,

917   Long, R. W., Szykman, J. J., Delgado, R., Thompson, A. M., Knepp, T. N., Lamsal, L. N., Janz, S. J.,

918   Kowalewski, M. G., Liu, X., and Nowlan, C. R.: Comprehensive evaluations of diurnal NO_2

919   measurements during DISCOVER-AQ 2011: effects of resolution-dependent representation of NO_x

920   emissions, Atmospheric Chem. Phys., 21, 11133–11160, https://doi.org/10.5194/acp-21-11133-2021,

921   2021.

922   Li, X., Wang, P., Wang, W., Zhang, H., Shi, S., Xue, T., Lin, J., Zhang, Y., Liu, M., Chen, R., Kan, H.,

923   and Meng, X.: Mortality burden due to ambient nitrogen dioxide pollution in China: Application of

924   high-resolution models, Environ. Int., 176, 107967, https://doi.org/10.1016/j.envint.2023.107967,

925   2023.

926   Lin, J.-T.: Satellite constraint for emissions of nitrogen oxides from anthropogenic, lightning and soil

927   sources over East China on a high-resolution grid, Atmospheric Chem. Phys., 12, 2881–2898,

928   https://doi.org/10.5194/acp-12-2881-2012, 2012.

929   Lin, J.-T., Martin, R. V., Boersma, K. F., Sneep, M., Stammes, P., Spurr, R., Wang, P., Van Roozendael,

930   M., Clémer, K., and Irie, H.: Retrieving tropospheric nitrogen dioxide from the Ozone Monitoring

931   Instrument: effects of aerosols, surface reflectance anisotropy, and vertical profile of nitrogen dioxide,

932   Atmospheric Chem. Phys., 14, 1441–1461, https://doi.org/10.5194/acp-14-1441-2014, 2014.

933   Lin, J.-T., Liu, M.-Y., Xin, J.-Y., Boersma, K. F., Spurr, R., Martin, R., and Zhang, Q.: Influence of

934   aerosols and surface reflectance on satellite NO_2 retrieval: seasonal and spatial characteristics and

Atmospheric
Measurement
Techniques
Discussions

935   implications for NO_x emission constraints, Atmospheric Chem. Phys., 15, 11217–11241,

936   https://doi.org/10.5194/acp-15-11217-2015, 2015.

937   Liu, M., Lin, J., Boersma, K. F., Pinardi, G., Wang, Y., Chimot, J., Wagner, T., Xie, P., Eskes, H., Van

938   Roozendael, M., Hendrick, F., Wang, P., Wang, T., Yan, Y., Chen, L., and Ni, R.: Improved aerosol

939   correction for OMI tropospheric NO_2 retrieval over East Asia: constraint from CALIOP aerosol

940   vertical profile, Atmospheric Meas. Tech., 12, 1–21, https://doi.org/10.5194/amt-12-1-2019, 2019.

941   Liu, M., Lin, J., Kong, H., Boersma, K. F., Eskes, H., Kanaya, Y., He, Q., Tian, X., Qin, K., Xie, P.,

942   Spurr, R., Ni, R., Yan, Y., Weng, H., and Wang, J.: A new TROPOMI product for tropospheric NO_2

943   columns over East Asia with explicit aerosol corrections, Atmospheric Meas. Tech., 13, 4247–4259,

944   https://doi.org/10.5194/amt-13-4247-2020, 2020.

945   Liu, O., Li, Z., Lin, Y., Fan, C., Zhang, Y., Li, K., Zhang, P., Wei, Y., Chen, T., Dong, J., and de Leeuw,

946   G.: Evaluation of the first year of Pandora NO_2 measurements over Beijing and application to satellite

947   validation, Atmospheric Meas. Tech., 17, 377–395, https://doi.org/10.5194/amt-17-377-2024, 2024a.

948   Liu, S., Valks, P., Pinardi, G., Xu, J., Chan, K. L., Argyrouli, A., Lutz, R., Beirle, S., Khorsandi, E.,

949   Baier, F., Huijnen, V., Bais, A., Donner, S., Dörner, S., Gratsea, M., Hendrick, F., Karagkiozidis, D.,

950   Lange, K., Piters, A. J. M., Remmers, J., Richter, A., Van Roozendael, M., Wagner, T., Wenig, M.,

951   and Loyola, D. G.: An improved TROPOMI tropospheric NO_2 research product over Europe,

952   Atmospheric Meas. Tech., 14, 7297–7327, https://doi.org/10.5194/amt-14-7297-2021, 2021.

953   Liu, S., Valks, P., Curci, G., Chen, Y., Shu, L., Jin, J., Sun, S., Pu, D., Li, X., Li, J., Zuo, X., Fu, W.,

954   Li, Y., Zhang, P., Yang, X., Fu, T.-M., and Zhu, L.: Satellite NO2 Retrieval Complicated by Aerosol

955   Composition over Global Urban Agglomerations: Seasonal Variations and Long-Term Trends (2001–

956   2018), Environ. Sci. Technol., 58, 7891–7903, https://doi.org/10.1021/acs.est.3c02111, 2024b.

957   Lorente, A., Folkert Boersma, K., Yu, H., Dörner, S., Hilboll, A., Richter, A., Liu, M., Lamsal, L. N.,

958   Barkley, M., De Smedt, I., Van Roozendael, M., Wang, Y., Wagner, T., Beirle, S., Lin, J.-T., Krotkov,

959   N., Stammes, P., Wang, P., Eskes, H. J., and Krol, M.: Structural uncertainty in air mass factor

960   calculation for NO_2 and HCHO satellite retrievals, Atmospheric Meas. Tech., 10, 759–782,

961   https://doi.org/10.5194/amt-10-759-2017, 2017.

962   Loyola, D. G., Gimeno García, S., Lutz, R., Argyrouli, A., Romahn, F., Spurr, R. J. D., Pedergnana, M.,

963   Doicu, A., Molina García, V., and Schüssler, O.: The operational cloud retrieval algorithms from

964   TROPOMI on board Sentinel-5 Precursor, Atmospheric Meas. Tech., 11, 409–427,

965   https://doi.org/10.5194/amt-11-409-2018, 2018.

966   Martin, R. V., Chance, K., Jacob, D. J., Kurosu, T. P., Spurr, R. J. D., Bucsela, E., Gleason, J. F., Palmer,

967   P. I., Bey, I., Fiore, A. M., Li, Q., Yantosca, R. M., and Koelemeijer, R. B. A.: An improved retrieval

968   of tropospheric nitrogen dioxide from GOME, J. Geophys. Res. Atmospheres, 107, ACH 9-1-ACH 9-

969   21, https://doi.org/10.1029/2001JD001027, 2002.

970   Richter, A. and Burrows, J. P.: Tropospheric NO2 from GOME measurements, Adv. Space Res., 29,

971   1673–1683, https://doi.org/10.1016/S0273-1177(02)00100-X, 2002.

Atmospheric
Measurement
Techniques
Discussions
Open Access
EGU

972 Richter, A., Burrows, J. P., Nüß, H., Granier, C., and Niemeier, U.: Increase in tropospheric nitrogen

973   dioxide over China observed from space, Nature, 437, 129–132, https://doi.org/10.1038/nature04092,

974   2005.

975 Rodgers, C. D. and Connor, B. J.: Intercomparison of remote sounding instruments, J. Geophys. Res.

976   Atmospheres, 108, https://doi.org/10.1029/2002JD002299, 2003.

977 Roujean, J.-L., Leroy, M., and Deschamps, P.-Y.: A bidirectional reflectance model of the Earth's

978   surface for the correction of remote sensing data, J. Geophys. Res. Atmospheres, 97, 20455–20468,

979   https://doi.org/10.1029/92JD01411, 1992.

980 Schaepman-Strub, G., Schaepman, M. E., Painter, T. H., Dangel, S., and Martonchik, J. V.: Reflectance

981   quantities in optical remote sensing—definitions and case studies, Remote Sens. Environ., 103, 27–

982   42, https://doi.org/10.1016/j.rse.2006.03.002, 2006.

983 Sen, P. K.: Estimates of the Regression Coefficient Based on Kendall's Tau, J. Am. Stat. Assoc., 63,

984   1379–1389, https://doi.org/10.1080/01621459.1968.10480934, 1968.

985 Shindell, D. T., Faluvegi, G., Koch, D. M., Schmidt, G. A., Unger, N., and Bauer, S. E.: Improved

986   Attribution of Climate Forcing to Emissions, Science, 326, 716–718,

987   https://doi.org/10.1126/science.1174760, 2009.

988 Stavrakou, T., Müller, J.-F., Bauwens, M., De Smedt, I., Van Roozendael, M., and Guenther, A.: Impact

989   of Short-Term Climate Variability on Volatile Organic Compounds Emissions Assessed Using OMI

990   Satellite Formaldehyde Observations, Geophys. Res. Lett., 45, 8681–8689,

991   https://doi.org/10.1029/2018GL078676, 2018.

992 Su, W., Liu, C., Chan, K. L., Hu, Q., Liu, H., Ji, X., Zhu, Y., Liu, T., Zhang, C., Chen, Y., and Liu, J.:

993   An improved TROPOMI tropospheric HCHO retrieval over China, Atmospheric Meas. Tech., 13,

994   6271–6292, https://doi.org/10.5194/amt-13-6271-2020, 2020.

995 Tilstra, G.: TROPOMI ATBD of the directionally dependent surface Lambertian-equivalent reflectivity,

996   2024.

997 Tilstra, L. G., de Graaf, M., Trees, V. J. H., Litvinov, P., Dubovik, O., and Stammes, P.: A directional

998   surface reflectance climatology determined from TROPOMI observations, Atmospheric Meas. Tech.,

999   17, 2235–2256, https://doi.org/10.5194/amt-17-2235-2024, 2024.

1000 Van Geffen, J., Boersma, K. F., Eskes, H., Sneep, M., ter Linden, M., Zara, M., and Veefkind, J. P.:

1001   S5P TROPOMI NO_2 slant column retrieval: method, stability, uncertainties and comparisons with

1002   OMI, Atmospheric Meas. Tech., 13, 1315–1335, https://doi.org/10.5194/amt-13-1315-2020, 2020.

1003 Van Geffen, J., Eskes, H., Compernolle, S., Pinardi, G., Verhoelst, T., Lambert, J.-C., Sneep, M., ter

1004   Linden, M., Ludewig, A., Boersma, K. F., and Veefkind, J. P.: Sentinel-5P TROPOMI NO_2 retrieval:

1005   impact of version v2.2 improvements and comparisons with OMI and ground-based data,

1006   Atmospheric Meas. Tech., 15, 2037–2060, https://doi.org/10.5194/amt-15-2037-2022, 2022a.

1007 Van Geffen, J. H. G. M., Eskes, H. J., Boersma, K. F., and Veefkind, P.: TROPOMI ATBD of the total

1008   and tropospheric NO2 data products version 2.4.0, 2022b.

1009   Vasilkov, A., Krotkov, N., Yang, E.-S., Lamsal, L., Joiner, J., Castellanos, P., Fasnacht, Z., and Spurr,
1010   R.: Explicit and consistent aerosol correction for visible wavelength satellite cloud and nitrogen
1011   dioxide retrievals based on optical properties from a global aerosol analysis, Atmospheric Meas. Tech.,
1012   14, 2857–2871, https://doi.org/10.5194/amt-14-2857-2021, 2021.

1013   Veefkind, J. P., Aben, I., McMullan, K., Förster, H., de Vries, J., Otter, G., Claas, J., Eskes, H. J., de
1014   Haan, J. F., Kleipool, Q., van Weele, M., Hasekamp, O., Hoogeveen, R., Landgraf, J., Snel, R., Tol,
1015   P., Ingmann, P., Voors, R., Kruizinga, B., Vink, R., Visser, H., and Levelt, P. F.: TROPOMI on the
1016   ESA Sentinel-5 Precursor: A GMES mission for global observations of the atmospheric composition
1017   for climate, air quality and ozone layer applications, Remote Sens. Environ., 120, 70–83,
1018   https://doi.org/10.1016/j.rse.2011.09.027, 2012.

1019   Verhoelst, T., Compernolle, S., Pinardi, G., Lambert, J.-C., Eskes, H. J., Eichmann, K.-U., Fjæraa, A.
1020   M., Granville, J., Niemeijer, S., Cede, A., Tiefengraber, M., Hendrick, F., Pazmiño, A., Bais, A.,
1021   Bazureau, A., Boersma, K. F., Bognar, K., Dehn, A., Donner, S., Elokhov, A., Gebetsberger, M.,
1022   Goutail, F., Grutter de la Mora, M., Gruzdev, A., Gratsea, M., Hansen, G. H., Irie, H., Jepsen, N.,
1023   Kanaya, Y., Karagkiozidis, D., Kivi, R., Kreher, K., Levelt, P. F., Liu, C., Müller, M., Navarro Comas,
1024   M., Piters, A. J. M., Pommereau, J.-P., Portafaix, T., Prados-Roman, C., Puentedura, O., Querel, R.,
1025   Remmers, J., Richter, A., Rimmer, J., Rivera Cárdenas, C., Saavedra de Miguel, L., Sinyakov, V. P.,
1026   Stremme, W., Strong, K., Van Roozendael, M., Veefkind, J. P., Wagner, T., Wittrock, F., Yela
1027   González, M., and Zehner, C.: Ground-based validation of the Copernicus Sentinel-5P TROPOMI
1028 NO_2 measurements with the NDACC ZSL-DOAS, MAX-DOAS and Pandonia global networks,
1029   Atmospheric Meas. Tech., 14, 481–510, https://doi.org/10.5194/amt-14-481-2021, 2021.

1030   Vigouroux, C., Langerock, B., Bauer Aquino, C. A., Blumenstock, T., Cheng, Z., De Mazière, M., De
1031   Smedt, I., Grutter, M., Hannigan, J. W., Jones, N., Kivi, R., Loyola, D., Lutsch, E., Mahieu, E.,
1032   Makarova, M., Metzger, J.-M., Morino, I., Murata, I., Nagahama, T., Notholt, J., Ortega, I., Palm, M.,
1033   Pinardi, G., Röhling, A., Smale, D., Stremme, W., Strong, K., Sussmann, R., Té, Y., van Roozendael,
1034   M., Wang, P., and Winkler, H.: TROPOMI–Sentinel-5 Precursor formaldehyde validation using an
1035   extensive network of ground-based Fourier-transform infrared stations, Atmospheric Meas. Tech., 13,
1036   3751–3767, https://doi.org/10.5194/amt-13-3751-2020, 2020.

1037   Wei, J., Liu, S., Li, Z., Liu, C., Qin, K., Liu, X., Pinker, R. T., Dickerson, R. R., Lin, J., Boersma, K.
1038   F., Sun, L., Li, R., Xue, W., Cui, Y., Zhang, C., and Wang, J.: Ground-Level NO_2 Surveillance from
1039   Space Across China for High Resolution Using Interpretable Spatiotemporally Weighted Artificial
1040   Intelligence, Environ. Sci. Technol., 56, 9988–9998, https://doi.org/10.1021/acs.est.2c03834, 2022.

1041   Williams, J. E., Boersma, K. F., Le Sager, P., and Verstraeten, W. W.: The high-resolution version of
1042   TM5-MP for optimized satellite retrievals: description and validation, Geosci. Model Dev., 10, 721–
1043   750, https://doi.org/10.5194/gmd-10-721-2017, 2017.

1044   Yombo Phaka, R., Merlaud, A., Pinardi, G., Friedrich, M. M., Van Roozendael, M., Müller, J.-F.,
1045   Stavrakou, T., De Smedt, I., Hendrick, F., Dimitropoulou, E., Bopili Mbotia Lepiba, R., Phuku Phuati,

E., Djibi, B. L., Jacobs, L., Fayt, C., Mbungu Tsumbu, J.-P., and Mahieu, E.: Ground-based Multi-AXis Differential Optical Absorption Spectroscopy (MAX-DOAS) observations of NO_2 and H_2CO at Kinshasa and comparisons with TROPOMI observations, Atmospheric Meas. Tech., 16, 5029–5050, https://doi.org/10.5194/amt-16-5029-2023, 2023.

Zhang, C., Liu, C., Chan, K. L., Hu, Q., Liu, H., Li, B., Xing, C., Tan, W., Zhou, H., Si, F., and Liu, J.: First observation of tropospheric nitrogen dioxide from the Environmental Trace Gases Monitoring Instrument onboard the GaoFen-5 satellite, Light Sci. Appl., 9, 66, https://doi.org/10.1038/s41377-020-0306-z, 2020.

Zhang, Y., Lin, J., Kim, J., Lee, H., Park, J., Hong, H., Van Roozendael, M., Hendrick, F., Wang, T., Wang, P., He, Q., Qin, K., Choi, Y., Kanaya, Y., Xu, J., Xie, P., Tian, X., Zhang, S., Wang, S., Cheng, S., Cheng, X., Ma, J., Wagner, T., Spurr, R., Chen, L., Kong, H., and Liu, M.: A research product for tropospheric NO_2 columns from Geostationary Environment Monitoring Spectrometer based on Peking University OMI NO_2 algorithm, Atmospheric Meas. Tech., 16, 4643–4665, https://doi.org/10.5194/amt-16-4643-2023, 2023.

Zhou, Y., Brunner, D., Spurr, R. J. D., Boersma, K. F., Sneep, M., Popp, C., and Buchmann, B.: Accounting for surface reflectance anisotropy in satellite retrievals of tropospheric NO_2, Atmospheric Meas. Tech., 3, 1185–1203, https://doi.org/10.5194/amt-3-1185-2010, 2010.